ACCELERATED DISTRIBUTION DEMONSTRATION SYSTEM

REGULATORY INFORMATION DISTRIBUTION SYSTEM (RIDS)

ACCESSION NBR:8903080423 DOC.DATE: 89/02/28 NOTARIZIED: NO DOCKET #
FACIL:50-275 Diablo Canyon Nuclear Power Plant, Unit 1, Pacific Ga 05000275
50-323 Diablo Canyon Nuclear Power Plant, Unit 2, Pacific Ga 05000323
AUTH.NAME AUTHOR AFFILIATION
SHIFFER,J.D. Pacific Gas & Electric Co.
RECIP.NAME RECIPIENT AFFILIATION
Document Control Branch (Document Control Desk)

See Rpt.

SUBJECT: Forwards licensee response to NRC 881213 questions on util long term siesmic program final rept.

DISTRIBUTION CODE: D031D COPIES RECEIVED:LTR 1 ENCL 1 SIZE: 48+5
TITLE: Diablo Canyon Long-Term Seismic Program

NOTES:

	RECIPIENT ID CODE/NAME	COPIES LTTR	COPIES ENCL	RECIPIENT ID CODE/NAME	COPIES LTTR	COPIES ENCL
	PD5 LA	1	0	PD5 PD	5	5
	ROOD,H	1	1			
INTERNAL:	ACRS	6	6	ADM/LFMB	1	0
	NRR ASHAR,H	1	1	NRR BAGCHI,G	1	1
	NRR JENG,D	1	1	NRR PICHUMANI,R	1	1
	NRR REITER,L	1	1	NRR ROTHMAN,R	1	1
	NRR/DEST/ADE 8H	1	1	NRR/DEST/ADS 7E	1	1
	NRR/PMAS/ILRB12	1	1	NUDOCS-ABSTRACT	1	1
	OGC/HDS2	1	0	REG FILE 01	1	1
	RES CHOKSHI,N	1	1	RES MCMULLEN,R	1	1
EXTERNAL:	LPDR	1	1	NRC PDR	1	1
	NSIC	1	1			

All Drawings To: Reg Files

Change: PDR 1 1, LPDR 1 1, NSIC 1 1 } NON-Prop Portion only

NOTE TO ALL "RIDS" RECIPIENTS:

PLEASE HELP US TO REDUCE WASTE! CONTACT THE DOCUMENT CONTROL DESK, ROOM P1-37 (EXT. 20079) TO ELIMINATE YOUR NAME FROM DISTRIBUTION LISTS FOR DOCUMENTS YOU DON'T NEED!

TOTAL NUMBER OF COPIES REQUIRED: LTTR 31 ENCL 28

M/A 2 cc

R I D S / A D D S

Pacific Gas and Electric Company

77 Beale Street
San Francisco, CA 94106
415/972-7000
TWX 910-372-6587

James D. Shiffer
Vice President
Nuclear Power Generation

February 28, 1989

PG&E Letter No. DCL-89-047

U.S. Nuclear Regulatory Commission
ATTN: Document Control Desk
Washington, D.C. 20555

Re: Docket No. 50-275, OL-DPR-80
Docket No. 50-323, OL-DPR-82
Diablo Canyon Units 1 and 2
Response to NRC Staff Questions on the
Long Term Seismic Program Final Report

Gentlemen:

Enclosed is PG&E's response to NRC questions of December 13, 1988, on the Diablo Canyon Long Term Seismic Program Final Report. This completes PG&E's response to the 47 questions asked by the NRC Staff.

Response to question 16,
Response to question 43n,
Part 2 of response to question 43z,
Response to question 46, and
Attachment Q43-5, Proprietary Common-depth-point Seismic Records, interpreted migrated sections

These responses have been distributed in accordance with the guidance provided by the NRC Staff on February 3, 1989.

Kindly acknowledge receipt of this material on the enclosed copy of this letter and return it in the enclosed addressed envelope.

Sincerely,

J. D. Shiffer

cc w/enc.: J. B. Martin
H. Rood

cc w/o enc.: M. M. Mendonca
P. P. Narbut
B. Norton
B. H. Vogler
CPUC
Diablo Distribution

2542S/0067K/DWO/1587

All Drawings
To: Reg Files

	Ltr	Encl	
Change PDR	1	1	Non Prop Portion only
LPDR	1	1	
NSIC	1	1	

D031 1/1

Pacific Gas and Electric Company

77 Beale Street
San Francisco, CA 94106
415/972-7000
TWX 910-372-6587

James D. Shiffer
Vice President
Nuclear Power Generation

February 28, 1989

PG&E Letter No. DCL-89-047

U.S. Nuclear Regulatory Commission
ATTN: Document Control Desk
Washington, D.C. 20555

Re: Docket No. 50-275, OL-DPR-80
Docket No. 50-323, OL-DPR-82
Diablo Canyon Units 1 and 2
Response to NRC Staff Questions on the
Long Term Seismic Program Final Report

Gentlemen:

Enclosed is PG&E's response to NRC questions of December 13, 1988, on the Diablo Canyon Long Term Seismic Program Final Report. This completes PG&E's response to the 47 questions asked by the NRC Staff.

Response to question 16,
Response to question 43n,
Part 2 of response to question 43z,
Response to question 46, and
Attachment Q43-5, Proprietary Common-depth-point Seismic Records, interpreted migrated sections

These responses have been distributed in accordance with the guidance provided by the NRC Staff on February 3, 1989.

Kindly acknowledge receipt of this material on the enclosed copy of this letter and return it in the enclosed addressed envelope.

Sincerely,

J. D. Shiffer

cc w/enc.: J. B. Martin
H. Rood

cc w/o enc.: M. M. Mendonca
P. P. Narbut
B. Norton
B. H. Vogler
CPUC
Diablo Distribution

Receipt of the above material is hereby acknowledged.
U.S. Nuclear Regulatory Commission

By _____
Date:

2542S/0067K/DWO/1587

RESPONSE TO QUESTIONS 43n, 43z (Part 2) and 46

February 1989

This volume is part of a set that responds to 47 questions asked of PG&E by the Nuclear Regulatory Commission (NRC) on December 13, 1988. The responses provide data requested to augment or clarify the Final Report of the Long Term Seismic Program submitted by PG&E to the NRC on July 31, 1988.

RESPONSE TO QUESTION 43n

QUESTION 43n

Provide the following:

n. The high resolution and CDP reflection profiles which show the style of deformation, continuity, and possible surface and subsurface position of segmentation points for the following:

(a) The Cambria step-over between the San Simeon and Hosgri faults.

(b) Estero Bay-Los Osos zone of deformation east of the Hosgri fault.

(c) Hosgri fault west of Pt. Buchon and Diablo Canyon.

(d) Offshore SW border of the Pismo block including seismic lines across the San Luis Bay-Rattlesnake trace, Olson trace, and offshore escarpments.

(e) Zone of intersection between the Hosgri and Pecho faults, including mid-points and gaps along the Pecho fault.

(f) Intersection of the Casmalia fault and Hosgri faults.

(g) Intersection of the Lion's Head fault and the Hosgri fault zone.*

(h) Southern termination of the Hosgri fault zone.*

**Items (g) and (h) have been added by PG&E to respond to Question 43f, which requests requests data on all the segmentation points within the framework of the response to Question 43n.*

This question requests offshore seismic data along the northern two-thirds of the Hosgri fault zone and along adjacent faults where they intersect the Hosgri fault zone (Figure Q43n-1). It overlaps, in whole or in part, data requested in the following questions:

- Question 41, which requests data regarding the northern termination of the Hosgri fault zone in the Cambria stepover area.
- Question 43a, which requests data regarding the Pecho fault and its role as a structural element along the southwestern margin of the San Luis/Pismo structural block.
- Question 43b, which requests data regarding the Pecho fault as it is associated with a segmentation point of the Hosgri fault zone.
- Question 43c, which requests data showing the relationship between the Los Osos and Hosgri fault zones.
- Question 43e, which, in part, requests data regarding near offshore faults in the vicinity of the Diablo Canyon Power Plant.
- Question 43f, which requests data regarding the six segmentation points of the Hosgri fault zone.
- Question 43g, which requests data regarding the southern termination of the Hosgri fault zone.

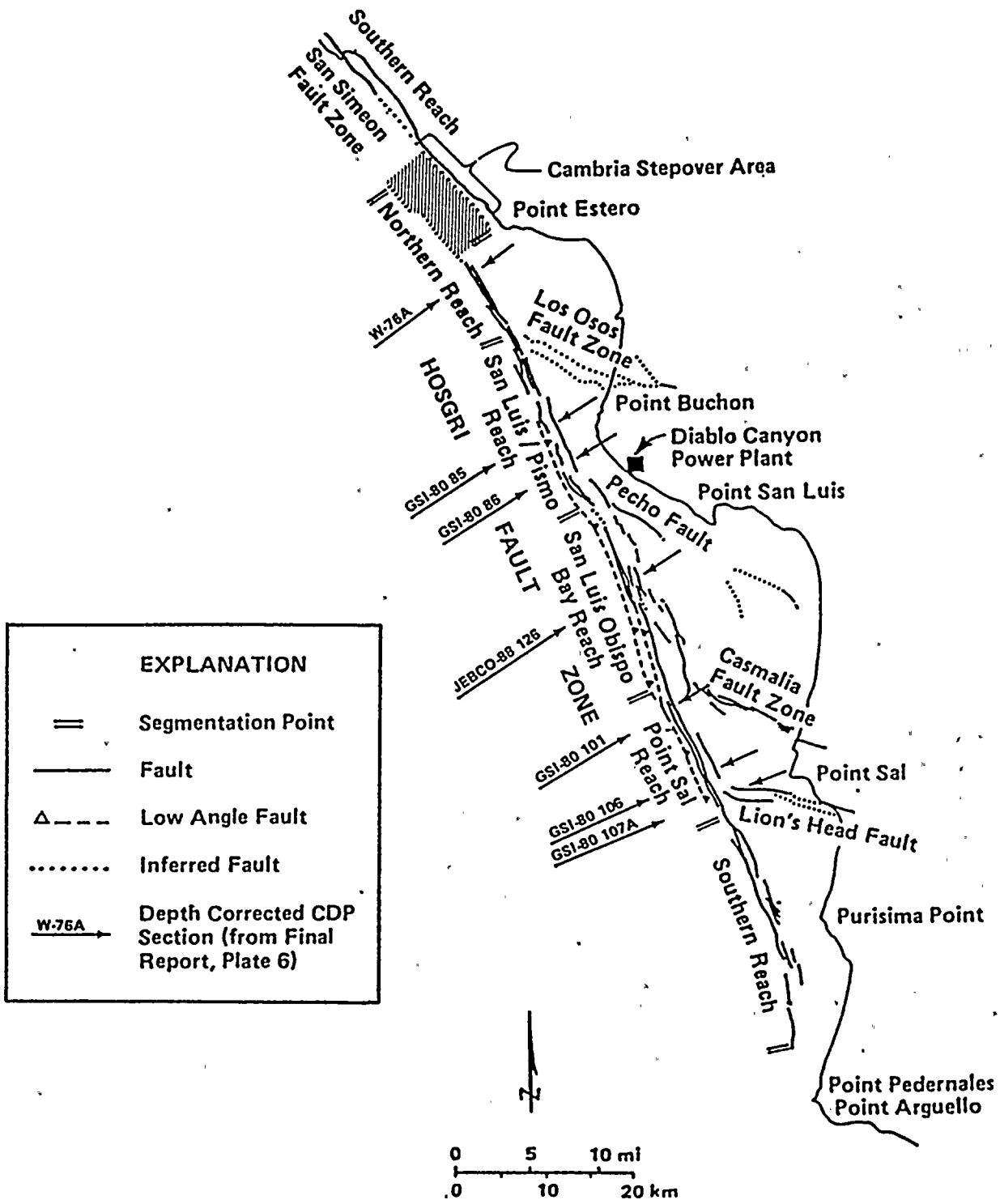

Figure Q43n-1

Segmentation points along the Hosgri fault zone (modified from Final Report Figure 2-42).

Separate responses have been provided for Questions 41, 43a, 43e, and 43g and are referenced in the response to this question. The responses for Questions 43b, 43c, and 43f are incorporated in this response to Question 43n. Sections 43n (g) and (h) have been added to provide a complete response to Question 43f as a part of the response to Question 43n.

Evaluation of Fault Segmentation

Fault segmentation is discussed in Chapter 3 of the Final Report (page 3-10 to 3-13). The assessment of fault segmentation is a geologic assessment that requires the integration of all available data sets that address the geometry, structural relationships, and behavior of a fault zone. For example, as discussed in the response to Question 41, the geologic interpretation for the existence of the Cambria stepover as a releasing stepover and point of segmentation along the San Simeon/Hosgri strike-slip fault zones is derived from the analyses of several data sets:

- theoretical and kinematic modeling studies to predict the nature of the geologic structures expected in a right-releasing stepover;
- geologic, geomorphic, and geophysical mapping to confirm the existence and termination points of the major bounding fault traces of the San Simeon and Hosgri fault zones;
- mapping based on high-resolution and common-depth-point seismic reflection data to identify local normal faults and down-dropped blocks within the stepover region;
- shallow geophysical investigations and structural contour mapping to identify local Quaternary basins within the stepover area, confirming extension within the stepover;
- detailed fault behavior studies of the onshore portion of the San Simeon fault zone to provide information on the style of deformation and timing of most recent rupture events on one of the bounding faults; and
- detailed geologic studies and case histories of surface rupture from other areas to provide data regarding the dimensional requirements (stepover width, basin development) necessary for considering a stepover as a possible segmentation point (for example, Sibson, 1986).

The above discussion demonstrates that the interpretation of segmentation of a fault zone is a *geologic* assessment that does not rely on any single data set, but integrates interpretations from theoretical, regional, and site-specific data and studies. The assessment of fault segmentation involves consideration of changes in fault behavioral and physical characteristics along strike, spatial separation of fault traces, relationship to intersecting faults and other structural elements, spatial association with local and regional changes in styles and rates of deformation, and other criteria. The geophysical data requested in this question provide a partial confirmation of the interpretation of segmentation on the Hosgri fault zone. Geologic data, for example geologic mapping in the San Luis/Pismo structural block and analysis of structures along its southwestern margin, are also integral parts of the segmentation interpretation.

Our interpretation of segmentation of the Hosgri fault zone is presented in Chapters 2 and 3 of the Final Report, in which geophysical and geologic data sets have been integrated. Based on studies of historical surface ruptures, fault characteristics of importance to segmentation are identified in Chapter 3 (pages 3-10 to 3-13; see also response to Question 43aa). With these studies as a basis, the segmentation of the Hosgri fault zone is evaluated and discussed in Chapter 2. On pages 2-96 to 2-98 (and associated plates) the segmentation points along the Hosgri fault zone are described in terms of their geometric and geologic characteristics. The fault traces between segmentation points are described on pages 2-98 to 2-105, drawing heavily, but not exclusively, on offshore geophysical data. On page 2-120 and Table 2-13, segments and their boundaries are described in terms of geometry, down-dip character, near-surface expression, and adjacent structures. Finally, implications of the segmentation of the Hosgri fault zone to possible rupture lengths are given on pages 3-23 to 3-24.

The Geophysical Data Base

The geophysical records requested in this question are provided in Attachments Q43-1 to Q43-5. Interpretations and observations along the nonproprietary seismic lines are tabulated in Attachments Q43-1 and Q43-2. The tabulation of the Hosgri fault zone observations on proprietary common-depth-point records is in Attachment Q43-3. The suite of uninterpreted common-depth-point seismic records is provided in Attachment Q43-4, and the interpreted versions of selected lines are found in Attachment Q43-5. Attachments Q43-3 to Q43-5 contain proprietary data and their distribution is limited.

In responding to this question, reference also has been made to the data and descriptions in the Final Report, (pages 2-96 to 2-105, Table 2-13, and Plates 5 and 6), and to the maps provided in response to Questions 43m and 43o (Plates Q43m-1, Q43m-2, Q43o-2, and Q43o-3).

Key interpretational observations regarding these data follow.

Responses to Question 43n, Parts (a) through (h)

(a) The Cambria step-over between the San Simeon and Hosgri fault zones.

These data are provided in the response to Question 41, which also provides data on the northern termination of the Hosgri fault zone and the southern termination of the San Simeon fault zone.

(b) Estero Bay-Los Osos zone of deformation east of the Hosgri fault zone.

The Los Osos fault zone intersects the Hosgri fault zone in the vicinity of 59-Meter Ridge (Final Report Figure 2-50). Geophysical data and work maps that illustrate the character of the Hosgri fault zone and the Los Osos fault zone at the intersection are provided in Attachment Q43-1, Sections 1 and 2; Attachment Q43-2, Section 12; Plate Q43o-3, Sheet 6; and Final Report Plates 5 and 6). These data show changes in both the strike and subsurface geometry of the Hosgri fault zone across the intersection with the Los Osos fault zone. Together with independent geologic and tectonic assessments of the slip rate and structural interaction with adjacent structural blocks, these geophysical data provide important physical and behavioral characteristics supporting segmentation of the Hosgri fault zone at this location.

59-Meter Ridge is located in the northwest corner of the San Luis/Pismo structural block between the converging trends of the Los Osos and Hosgri fault zones. It is a structurally complex area of elevated Tertiary bedrock having a surface expression consisting of three parallel ridges that strike about N60°W (Attachment Q43-2, Section 12, Figure LO-2; Attachment Q43l, Plate 1). The tallest of these ridges is as shallow as 59 meters below sea level. Rock samples dredged from 59-Meter Ridge are mostly cherty siltstone with traces of asphaltum and are similar to rocks onshore from the upper Obispo and lower Monterey Formations (D. Clark, 1989, personal communication).

South of 59-Meter Ridge, the San Luis/Pismo reach of the Hosgri fault zone strikes N25°W for 22 ± 1 kilometers (Plate Q43o-3, Sheet 6; Figure Q43n-1; and Final Report Table 2-13). Along this reach, the Hosgri fault zone forms the western boundary of the highly deformed San Luis/Pismo structural block (Attachment Q43-1, Section 13, Figures H-14 and H-34). The Hosgri fault zone is generally 2 kilometers wide in this reach and is composed of three structural elements: a western trace that is near-vertical to vertical in the upper 1 kilometer, and dips 65 to 70 degrees northeast at depths of 3 to 4 kilometers; an eastern trace that dips 70 to 80 degrees northeast; and a low angle fault that dips 40 to 50 degrees northeast (Final Report Plate 6; Plates Q43k-2 and -3; Attachment Q43-1, Section 3, Figures H-17 and H-23).

North of 59-Meter Ridge and the intersection with the Los Osos fault zone, the strike of the Hosgri fault zone is more northwesterly, N40°W (parallel to the San Simeon fault zone), and the fault zone becomes less than 1 kilometer wide. The low-angle fault dies out south of 59-Meter Ridge and the

intersection with the Los Osos fault zone. West Trace No. 1 dies out at 59-Meter Ridge, just south of the Los Osos fault zone. East Trace No. 1 changes geometry across the intersection with the Los Osos fault zone. To the south, the trace dips to the east; to the north, it is near-vertical to vertical, showing much the same geometry as West Trace No. 1. East Trace No. 1 continues northwest about 5 kilometers beyond the Hosgri/Los Osos intersection, and then dies out (Plate Q43o, Sheet 6). From this point, at the latitude of mid-Estero Bay, north to the Cambria stepover, there is only one Hosgri fault trace, the North Trace, which does not extend south of the intersection with the Los Osos fault zone.

The Los Osos fault zone forms the northeastern boundary of the San Luis/Pismo structural block (Final Report Figure 2-11). It coincides with a prominent range front on land in the Irish Hills area; its topographic expression diminishes to the northwest near Morro Bay. Except within about 5 kilometers of the intersection with the Hosgri fault zone, there is no bathymetric evidence for the Los Osos fault (Attachment Q43-2, Section 12, Figures LO-7, LO-10, and LO-13). Although the exact nature of the interaction between the Hosgri and Los Osos fault zones is not well imaged, the relief of 59-Meter Ridge, including a 20-meter scarp on its southwestern side (Figure LO-1) strongly suggests that northeast/southwest compression has been operative across the intervening region between the two converging fault zones (Figure LO-3).

(c) Hosgri fault west of Pt. Buchon and Diablo Canyon.

The 22-km-long portion of the Hosgri fault zone between the intersection of the Los Osos fault zone to the north and the Pecho fault to the south is referred to as the San Luis/Pismo reach (Figure Q43n-1). The characteristics of this reach are discussed in the Final Report on pages 2-101 to 2-103 and are summarized in Table 2-13 (page 2-121).

Detailed mapping of this reach of the Hosgri fault zone is shown on Plate Q43o-3, Sheets 5 and 6. Observations of the various fault traces on the nonproprietary data sets are tabulated in Attachment Q43-1, Sections 2, 3, 4, and 13. Interpretations based on proprietary common-depth-point seismic reflection data are summarized in Attachment Q43-3; complete record sections are provided in Attachment Q43-4 (uninterpreted) and Attachment Q43-5 (interpreted). Bathymetric data across this reach of the Hosgri fault zone are presented on Plate 2 of Attachment Q43l-1. The post-late Wisconsinan sediment isopach horizon is shown on Plate Q43o-2 (Sheets 5 and 6) and the work maps showing structural contours and associated isochrons on the deeper horizons are found in Plates Q43y-1 to Q43y-10. Shipborne gravity data and aeromagnetic data are shown on Plates Q43m-1 and Q43m-2, respectively.

Beginning at the southern end of the San Luis/Pismo reach, the general trend of the Hosgri fault zone bends approximately five degrees to the west (from N20°W to N25°W). West of Point Buchon, it follows a more northerly trend before again turning northwest at the intersection with the Los Osos fault zone. This geometry in a right-slip fault is a left-restraining bend that is coincident with the western margin of the uplifting San Luis/Pismo structural block.

The Hosgri fault zone along this reach consists of several high-angle traces, generally within a 2-kilometer-wide zone, and a low-angle trace, 1 to 2 kilometers west of the high-angle traces. The down-dip relationships between the three fault traces are shown on the depth-corrected sections for lines GSI-85 and -86 (Final Report Plate 6). A 15-kilometer-long anticlinal fold has been mapped between the west and east traces of the Hosgri fault zone over the southern two-thirds of the San Luis/Pismo reach. The rocks involved in the pre-mid-Pliocene history of this fold are most intensely deformed just south of the latitude of Point Buchon (Attachments Q43-4 and Q43-5, lines CM86-15 and -17). Upwarping of the mid-Pliocene unconformity is also pronounced (Plate Q43y-1). Moving south to the intersection of the Hosgri fault zone and the Pecho fault, the intensity of deformation rapidly diminishes (Attachments Q43-4 and Q43-5, lines CM86-15, -13, -119 and -117).

(d) Offshore SW border of the Pismo block including seismic lines across the San Luis Bay-Rattlesnake trace, Olson trace, and offshore escarpments.

Discussion of the offshore southwestern boundary of the San Luis/Pismo structural block is presented in the response to Question 43a. Identification of the area of intersection of the Pecho fault and the Hosgri fault zone as a potential Hosgri segmentation point is discussed in part (e) of this response. Discussions of offshore escarpments along the San Luis/Pismo reach of the Hosgri fault zone are presented in the response to Question 43l. Observations of fault characteristics based on high-resolution geophysical data for the San Luis Bay and Olson faults are found in Attachment Q43-2, Sections 14 and 15. Proprietary common-depth-point seismic reflection data are presented in Attachments Q43-4 and Q43-5. Plate Q43o-3, Sheet 5 is a work map based on all these data.

(e) Zone of intersection between the Hosgri and Pecho faults, including mid-points and gaps along the Pecho fault.

The area of intersection of the Pecho fault with the Hosgri fault zone is considered to be a potential segmentation point because it separates the San Luis/Pismo reach of the fault zone to the north from the San Luis Obispo Bay reach of the fault zone to the south (Figure Q43n-1 and Final Report page 2-98). Each reach of the fault zone is observed to be distinct from adjacent reaches, as indicated by differences in fault characteristics (Final Report Table 2-13). The San Luis Obispo Bay reach differs from the San Luis/Pismo reach (see response to part (b) of this question and Final Report pages 2-101 to 2-103) in that it is as wide as 3.4 kilometers and typically has one or more intermediate traces between the west and east traces of the fault zone (Attachment Q43-2, Section 12, especially Figures H-69 and H-71; and Q43o-3, Sheets 4 and 5). The San Luis Obispo Bay reach is also unique along the Hosgri fault zone in that two prominent low-angle faults are associated with and lie directly west of the fault zone in this area (Final Report Plates 5 and 6, and Figure Q43n-1). Where the low-angle faults are included, the Hosgri fault zone is as wide as 6.5 kilometers, by far the widest part of the entire fault zone.

Beginning at the southern end of the San Luis/Pismo reach, there is a left-restraining bend in the Hosgri fault zone (Final Report Plate 5, Sheet 2; Plate Q43o-3, Sheet 5; and Attachments Q43-4 and 5, lines GSI-85, -86, -87A, -89, -93, and -94). A prominent fold that deforms the mid-Pliocene unconformity is also present in this area (Plate Q43y-1). Both the deflection of the fault traces and the fold are the result of compression. The compression may be the result of either uplift and impingement of the San Luis/Pismo structural block east of the Hosgri fault zone, or continuing Hosgri fault displacement through a left-restraining bend. No similar deformation is observed west of the San Luis Obispo Bay reach, south of the Pecho fault intersection.

The Pecho fault is a northwest-trending fault that is one of the structural elements along the southwestern margin of the San Luis/Pismo structural block (see response to Question 43a and Attachment Q43-2, Section 16). The Pecho fault is mapped to within 0.5 kilometer of the eastern trace of the Hosgri fault zone approximately 4 kilometers southwest of the Diablo Canyon Power Plant. However, the available data do not permit imaging the exact nature of the intersection. It cannot be determined whether the Pecho fault dies out, merges with, or is truncated by the eastern trace of the Hosgri fault zone (Plate Q43o-3, Sheet 5; Attachment Q43-1, Section 4). A more complete discussion of the data base for the Pecho fault, including reference to apparent gaps in its near-surface continuity, is given in the response to Question 43a.

(f) Intersection of the Casmalia and Hosgri fault zones.

The Casmalia and Hosgri fault zones interact in an area that is characterized by numerous short (typically 1.5 kilometer long) folds and fault traces that have strikes intermediate between that of the Hosgri fault zone (N20°W) and that of the Casmalia fault zone (N65°W). The Casmalia fault zone bends northward to become subparallel to the Hosgri fault zone before dying out after an overlap of 2 to 3 kilometers (Attachment Q43-2, Section 20; Q43o-3, Sheets 3 and 4; Final Report Plate 5, Sheets 1 and 2). It does not appear to intersect or merge with the Hosgri fault zone

(Attachments Q43-4 and Q43-5, line 45-200, shot points 104 to 124). In addition to geologic and tectonic considerations that support a change in slip rate along the Hosgri fault zone in this area (Final Report pages 2-33 to 2-36), geophysical data indicate that the physical character of the fault zone changes abruptly across the intersection with the Casmalia fault zone (Attachment Q43-3, lines GSI-97, -101, and -103). This region also marks the transition from the San Luis Obispo Bay reach of the Hosgri fault zone to the north (see response to Question 43n(e)) to the Point Sal reach to the south (Figure Q43n-1; Final Report Table 2-13 and page 2-103).

As described in the response to question 43n (e), the San Luis Obispo Bay reach is characterized by a continuous western trace, a discontinuous eastern trace and several intermediate traces in a zone up to 3.4 kilometers wide. The Point Sal reach of the Hosgri fault zone is characterized by a single continuous western trace. The eastern trace mapped along the San Luis Obispo Bay reach does not extend south of the Casmalia fault, as evidenced by a prominent, 6-kilometer-long syncline parallel to the Casmalia trend that extends unbroken across its southeastern projection (Final Report Plate 5, Sheet 1). The syncline is interpreted to lie along the margin of the offshore Santa Maria Basin, and although the basin at latitudes north of Point Sal is generally not affected by tectonism east of the Hosgri fault zone, this syncline appears to be related to compression associated with the Casmalia block (Final Report Figure 2-8). Another eastern trace of the Hosgri fault zone begins 2.5 kilometers south of the syncline and the zone of intersection with the Casmalia fault zone.

The Casmalia fault zone is observed on seismic records as a west-northwest-trending, southwest-dipping complex of reverse faults and folds (Attachment Q43-2, Section 20, Figures C-5, C-6, and C-9). The primary fault consists of two major traces, one 3.5 kilometers long and one 6 kilometers long, that dip about 50 degrees southwest. There are also several shorter fault traces, as well as numerous subparallel folds (Figures C-10, C-11). On shallow, high-resolution seismic reflection data, the Casmalia fault zone is imaged as a tight kink fold in upwarped Tertiary sediments (Figure C-4). This folding resembles the onshore geology a few kilometers to the southeast, where the Monterey Formation is deformed sharply upward and fluvial gravel beds of the Pliocene and Pleistocene Paso Robles Formation are locally overturned in the hanging wall of the fault. Onshore drilling data suggest the Casmalia fault zone is a major structure that vertically separates both the Franciscan assemblage basement and the overlying Tertiary section by several hundred meters. The amount of vertical separation across the Casmalia fault zone offshore diminishes from approximately 70 meters (79 meters using a sound velocity of 2250 meters per second) near the shoreline to virtually zero near the Hosgri fault zone to the northwest (Figures C-1, C-2, C-7, C-9; Attachment Q43-4, lines 45-200 and 45-202).

(g) Intersection of the Lion's Head fault and the Hosgri fault zone.

The intersection of the Lion's Head fault with the Hosgri fault zone is considered to be a segmentation point of the Hosgri fault zone. At the intersection, the sense of vertical separation of basement across the Hosgri fault zone changes from east side up to the north, to west side up to the south (see response to Question 43h). There is no apparent interaction between the Hosgri fault zone and the Lion's Head fault and associated structures. The Lion's Head fault does not extend into the Hosgri fault zone, nor does it bend significantly as it approaches the Hosgri fault zone (Plate Q43o-3, Sheet 3; Attachment Q43-2, Sections 21 and 22).

This segmentation point separates the Point Sal reach of the Hosgri fault zone to the north from the southern reach of the Hosgri fault zone (Figure Q43n-1; Plate Q43o-3, Sheet 3). The southern reach differs from other reaches of the Hosgri fault zone in that neither the western nor the eastern trace clearly marks the eastern limit of the offshore Santa Maria Basin (Attachment Q43-1, Section 7, Figures H-83 and H-84, and Section 8, Figure H-86). Rather, the fault traces lie within a section of raised and folded sediment of probable middle Tertiary age (compare Attachment Q43-1, Sections 6 and 13 with Sections 7, 8, and 14). In addition, the southern reach truncates several east-west-trending folds that bend to the south as they approach the eastern side of the Hosgri fault zone (Attachment Q43-2, Section 23; Plate Q43o-3, Sheet 3).

(h) Southern termination of the Hosgri fault zone.

The southern termination of the Hosgri fault zone near Point Pedernales is a segmentation point because the fault zone is interpreted to end as a through-going structural feature. Details of the southern termination of the Hosgri fault zone are presented in the response to Question 43g.

References

Sibson, R. J., 1986, Rupture interaction with fault jogs: in Earthquake Source Mechanics, Ewing Symposium: American Geophysical Union Monograph 37, p. 157-167.

RESPONSE TO QUESTION 43z
(Part 2)

QUESTION 43z (Part 2)

Provide the following:

z. Draft reports and seismic reflection data (including high resolution profiles) for the style, rates and timing of deformation on the section across the Queenie structure to the Pt. Sal area, and also for the Lompoc structure.

A draft report and related data compilation regarding the Queenie structure were presented as a pre-publication manuscript in Attachment Q43z-1 in the response to NRC questions dated January 1989.

Our investigations of the Lompoc structure did not involve the same level of detail as those of the Queenie structure, and no manuscript on the style, rates, and timing of deformation has been produced. The regional structural pattern and the position of the Lompoc structure are shown on Plate 5, sheet 1 of the Final Report.

Bathymetric and geophysical data across the Lompoc structure were mapped and interpreted during the Long Term Seismic Program, and are discussed in Attachment Q43z-2, which follows. The seismic data and interpretive maps are provided as plates and attachments prepared in response to other questions as follows:

- Geophysical Survey Line Maps: Plates Q43o-1a and 1b, Sheets D-2 and D-3
- Common-Depth-Point Seismic Records: Uninterpreted Sections: Attachment Q43-4
  Interpreted Sections: Attachment Q43-5
- Gravity Map: Plate Q43m-1, Sheet 1
- Near-Surface Faults and Thickness of Post-Late Wisconsinan Sediments Map: Plate Q43o-2, Sheets D-2 and D-3
- Structural Trend Map: Plate Q43o-3, Sheets D-2 and D-3
- Stucture Contour Work Maps: Plates Q43y-1, -2, and -3
- Isochron Work Maps: Plates Q43y-4 to -10.

ATTACHMENT Q43z-2

SEISMIC REFLECTION DATA ACROSS THE OFFSHORE LOMPOC STRUCTURE

The offshore Lompoc structure consists of an en echelon pair of anticlines that form a prominent fold trend within the southeastern part of the offshore Santa Maria basin approximately 20 kilometers west-northwest of Purisima Point (see Plate 5, sheet 1 of the Final Report). The structure has an average trend of N35°W and is about 25 kilometers long. It aligns along strike with another anticline, here referred to as the Pedernales structure, located 7 kilometers to the southeast. The overall length of the combined offshore Lompoc and Pedernales fold trend is about 45 kilometers. The eroded crest of the Lompoc structure, consisting of upper Miocene and lower Pliocene strata of the Sisquoc Formation, forms a distinctive series of subparallel sea floor ridges along the southern 12 kilometers of the Lompoc structure. The structure also marks a distinct bathymetric and structural inflection of the seafloor; the slope of the seafloor steepens to the southwest across much of the fold trend. The offshore Lompoc structure and the aligned Pedernales structure thus define the break between a gently west-dipping nearshore shelf platform area and a slightly steeper surface in the outer basin. Structurally, the Lompoc structure lies between a pair of synclinal basins that are in turn bordered by the Queenie structure on the west (see Attachment Q43z-1) and by the Purisima structure on the east (Plate 5, sheet 1 of the Final Report).

The Lompoc structure is imaged in several geophysical data sets. We have constructed a bathymetric map of the Lompoc structure from available geohazard reports filed for petroleum lease blocks in the area (Plate 1). A grid of Geophysical Service Incorporated (GSI) common-depth-point (CDP) seismic reflection data obtained by PG&E provide information on deeper structure; high-resolution Fairfield and Fugro seismic reflection data (Table 2-3 of the Final Report) image shallow structure. Attachment Q43-4 presents uninterpreted sections of the GSI CDP seismic lines, and Attachment Q43-5 presents interpreted versions of most of the GSI CDP lines that cross the Lompoc structure. Copies of the high-resolution seismic records from the Fairfield survey that were collected in the vicinity of the GSI CDP seismic lines are presented in Figures 1 to 12 of this attachment.

Bathymetry and Shallow Structure

Plate 1 is a bathymetric map having a 5-meter contour interval. It was compiled from available geohazard studies of offshore lease blocks, and shows the seafloor expression of the Lompoc structure. The bathymetric contours reflect the north-northwest-trending structural grain of the Lompoc structure and the en echelon character of the fold trend. The bathymetry also illustrates the erosional planation of the crest of the structure, which is imaged in the seismic data described below.

Common-Depth-Point and High-Resolution Seismic Reflection Data

In the following paragraphs, we describe interpreted versions of GSI CDP seismic reflection sections that cross the Lompoc structure (Attachment Q43-5). These lines cross the structure roughly perpendicular to the north-northwest-trending structural grain. Tie lines GSI-98, -99, and -99A, which trend roughly parallel to the structural grain, are also presented in Attachment Q43-5. Copies of east-west oriented high-resolution seismic sections from the Fairfield data set also are presented. These vertically exaggerated (about 11:1) sections provide constraints on the structure of the youngest sediments (late Pliocene and Pleistocene in age) that cover the Lompoc structure. Typically, east of the Lompoc structure, the upper 0.01 to 0.02 seconds of sediments in the Fairfield data set appear to form a relatively undeformed packet of deposits. Because of the unconformable relationship of these deposits with the underlying sediments, we have mapped the upper packet of deposits as post-Late Wisconsinan in age (Plate Q43o-2). The geographic locations of the GSI and Fairfield survey lines are shown in Plate Q43o-1b, sheets D2. The locations of the survey lines relative to the mapped structures in the vicinity of the Lompoc structure are shown in Plate Q43o-3, sheets D2 and D3.

Line GSI-104

GSI-104 extends from the Queenie structure on the southwest to the Hosgri fault zone on the northeast, directly northwest of the northwestern end of the Lompoc structure. The northeastward downwarp in basement between shot points 550 and 700 coincides with the northwestward projection of the Lompoc structure, and is a feature that is expressed throughout most of the length of the Lompoc structure. Southwest-dipping faults in the basement at shot points 600 and 650 are interpreted to underlie this downwarp. Northeast-dipping faults east of shot point 920 occur beneath the northwestern end of the Purisima structure. The structures disrupt pre-Pliocene units and partially deform lower Pliocene units. The absence of measurable deformation of post-mid-Pliocene units, however, indicates that there has been little or no activity on these structures at this latitude since early Pliocene time.

Lines GSI-105 and Fairfield SM-120

GSI-105 depicts the northwesternmost part of the Lompoc structure within the Neogene section between shot points 250 and 400. An angular unconformity within Miocene units at shot point 310 at 1.6 seconds depth indicates that structural deformation occurred during the Miocene Period; the relatively uniform thickness of beds in the upper part of the Miocene section imaged in this reach of the seismic line suggests that the beds were deposited over a region of relatively low relief. The angular truncation across the top Miocene unconformity at shot point 310 and the onlap and slight deformation of the overlying lower Pliocene units indicate that deformation occurred between the late Miocene and the late Pliocene. Upper Pliocene units are slightly warped over the structure in high-resolution line SM-120 (Figure 1, shot point 177) but the Pleistocene units that form the most recent deposits do not appear to be disturbed. A southwest-dipping fault interpreted within the basement underlies the northeast-facing step-down in basement and pre-mid-Pliocene sediments, although the fold geometries suggest that the system of faulting in the basement may be more complex.

Lines GSI-106 and Fairfield SM-118

Most of the structural elements of the northernmost part of the Lompoc structure imaged in line GSI-105 are also imaged in line GSI-106 (GSI-106, shot points 600 to 800): the angular unconformity within the Miocene section, a relatively uniform bedding thickness in the upper part of the Miocene section, the locally angular discordance across the top Miocene unconformity, the southwestward onlap of lower Pliocene units onto Miocene units, the slight and upwardly diminishing deformation of Pliocene units, and the apparent absence of deformation of the capping Pleistocene units (Figure 2, shot points 171 to 187). A southwest-dipping basement fault similar to that shown in line GSI-105 is interpreted to lie beneath the Lompoc structure in line GSI-106.

Lines GSI-107 and Fairfield SM-116

On line GSI-107, the Lompoc structure is a prominent northeast-vergent fold in pre-upper Pliocene units (shot points 330 to 510). Although no distinct mid-Miocene unconformity similar to the unconformity imaged in lines GSI-105 and 106 occurs in line GSI-107, the lower part of the Miocene section appears to thin dramatically within the Lompoc structure. Again, the upper half of the Miocene section does not appear to thin greatly over the structure, indicating low relief when those beds were deposited. Unlike the deformation imaged in the GSI lines to the northwest, the fold imaged in line GSI-107 appears to fully involve the lowest portion of the lower Pliocene units (that is, they appear conformable with the subjacent Miocene units). The middle and upper portions of the lower Pliocene section lap onto the Lompoc structure, and are partially involved in the deformation. High-resolution line SM-116 (Figure 3, shot points 175 to 185) suggests that upper Pliocene units are slightly warped, and that the Pleistocene units and the seafloor are not disturbed. A series of southwest-dipping faults is imaged in the upper basement and lower Neogene units beneath the Lompoc structure. Basement reflectors and the east-vergent asymmetry of the Lompoc structure in line GSI-107 both suggest that several west-dipping basement reverse faults underlie the Lompoc structure.

Lines GSI-108A and Fairfield SM-114

On line GSI-108A, the Lompoc structure maintains a generally northeast-vergent sense of asymmetry (shot points 400 to 530) similar to that imaged on line GSI-107. The lower part of the Miocene section again thins across the structure, and the upper part of the Miocene section does not. Similarly, the lower portion of the lower Pliocene section does not appear to thin over the crest of the structure, whereas upper units of the lower Pliocene section clearly lap onto the fold and are themselves folded. High-resolution data (Figure 4, shot points 173 to 184) indicate that upper Pliocene units are folded. A slight inflection of the seafloor is noted at shot point 181 (Figure 4). This inflection may be a result of Pleistocene or Holocene folding, incomplete infilling or differential sediment compaction across an older structure, or erosion. Weak reflectors in the basement beneath the fold suggest that one or more southwest-dipping faults similar to those in line GSI-107 are present.

Lines GSI-112C and Fairfield SM-112

The Lompoc structure becomes more complex in line GSI-112C (shot points 364 to 530). The structure consists of three anticlines superimposed on the overall up-to-the-southwest step in basement and Miocene units. The superimposed anticlines do not have a clear sense of asymmetry, although the larger southwest-side-up step indicates that the southwest side of the Lompoc structure has been uplifted relative to the basin to the northeast. Reflectors in the basement and lower sedimentary section suggest that east-dipping faults may underlie the smaller folds. As interpreted in this seismic section, the local structural relief of the top of basement unconformity beneath the Lompoc structure is significantly less than that of the top Miocene unconformity. This relationship is repeated in most of the interpreted seismic lines across the Lompoc structure south of line GSI-112C. When combined with the generally southwest-vergent asymmetry of the folds in the Neogene section, this observation indicates that the Miocene units beneath the fold have been structurally thickened by southwest-vergent bedding-plane faulting.

Lower Pliocene units appear to lap onto the Lompoc structure and are partially folded. Fairfield line SM-112 (Figure 5, shot points 179 to 194) indicates that upper Pliocene units are also folded across the structure, although is is not clear whether Pleistocene deposits are disturbed. Figure 5 (shot points 194 to 203) and GSI-112C (shot points 550 to 630) show that post-Miocene sediments and the seafloor within the basin bounding the Lompoc structure to the east are slightly warped.

Lines GSI-113A and Fairfield SM-108

In line GSI-113A, the Lompoc structure is southwest-vergent within the Neogene section, and the overall sense of uplift across the fold suggests southwest side up (shot points 310 to 500). Again, local structural relief of the top of basement unconformity is significantly less than that of the top Miocene unconformity, suggesting bedding-plane faulting originating to the northeast of the structure. Basement reflectors can be interpreted to show northeast-dipping faults within the deeper core of the Lompoc structure. Line GSI-113A is the northernmost line in which the crest of the Lompoc structure breaks the seafloor. Lower Pliocene units lap onto the fold and are deformed. Upper Pliocene deposits are also folded, but poor imaging of the Pleistocene deposits obscure the assessment of post-Pliocene deformation (Figure 6, shot points 165 to 179). Line GSI-113A is the northernmost section in which the Lompoc structure marks the point of inflection of the sea floor between a gentle gradient (about 0.5 degrees) to the northeast and a slightly steeper gradient (about 0.7 degrees) to the southwest (see also Plate 1 and Figure 7). This relationship continues to the southeast, where the gradient change becomes slightly more pronounced.

Lines GSI-114 and Fairfield SM-104

The Lompoc structure persists as a southwest-vergent fold within the Neogene section in line GSI-114 (shot points 350 to 500); the overall sense of separation across the structure indicates southwest side up. As with the adjacent sections to the north, the local structural relief of the top Miocene unconformity is interpreted to be substantially greater than that of the top of basement unconformity

beneath the Lompoc structure, again indicating that bedding-plane slip has caused structural thickening of the lower part of the Miocene section. The southwest-vergent asymmetry of the shallower levels of the Lompoc structure suggests that the bedding-plane faulting originates to the northeast. A northeast-dipping basement fault disrupts the core of the anticline, and a southwest-dipping reverse fault appears to offset the base of the Tertiary section at the base of the eastern limb of the structure. Lower Pliocene units lap onto the Lompoc structure and are folded, as are upper Pliocene units (line SM-104, Figure 7, shot points 195 to 210). Figure 7 also suggests that Pleistocene deposits on the limbs of the structure are not folded.

Lines GSI-115 and Fairfield SM-102

In line GSI-115, the Lompoc structure has three crests: a prominent northeastern anticline that reaches the seafloor, and two smaller southwestern anticlines (shot points 270 to 470). The sense of asymmetry, the difference in local structural relief between the Miocene and basement unconformities, and the timing of folding on the prominent northeastern fold of the structure (shot points 350 to 470) are similar to those imaged in line GSI-114. High-resolution line SM-102 (Figure 8, shot points 168 to 175) indicates that Pleistocene deposits northeast of the Lompoc structure truncate folded upper Pliocene deposits, and are not themselves folded.

Lines GSI-116 and Fairfield SM-96

In line GSI-116, the Lompoc structure has a lower amplitude than that imaged on the northern sections, and the single-crested anticline has been replaced by three smaller-amplitude anticlines that are each roughly symmetrical (shot points 250 to 410). We interpret the difference between the local structural relief of the top of basement unconformity and the top Miocene unconformity within the Lompoc structure to persist in this line. Lower Pliocene units lap onto the structure and are also folded. High-resolution line SM-96 (Figure 9, shot points 1155 to 1173) indicates that upper Pliocene units have been folded. Pleistocene deposits are absent or not well imaged in Figure 9. At shot point 300 on line GSI-116, upper Pliocene units and the seafloor appear to mimic the underlying anticline/syncline pair, suggesting possible Pleistocene or Holocene deformation. GSI-116 also shows that the overall southwest-side-up relationship of basement and Miocene units across the structure is present in this area, similar to the lines to the north.

Lines GSI-118 and Fairfield SM-92

In line GSI-118, the Lompoc structure forms a single-crested, southwest-vergent anticline above an up on the southwest step in basement (shot points 260 to 390). The nonalignment of the hinge lines of the anticlines at shot points 305 and 285 at 1-second depth suggests that the folds are separate structures. This relationship provides evidence for structural thickening of the Miocene section via southwest-directed bedding-plane or flexural-slip faulting. Lower Pliocene sediments partially lap onto and thin over the crest of the structure. High-resolution seismic line SM-92 (Figure 10, shot points 1155 to 1178) shows that upper Pliocene units are folded. Although Pleistocene deposits northeast of the Lompoc structure do not appear to be folded, an inflection in the seafloor southwest of the Lompoc structure between shot points 1160 and 1163 (Figure 10) may reflect late Pleistocene or Holocene folding.

Lines GSI-120 and Fairfield SM-82

The Lompoc structure has a very slight southwest-vergent sense of asymmetry in line GSI-120 (shot points 200 to 300). Our interpretation of this line shows that a step in basement is absent beneath the structure. Based on this interpretation, substantial bedding-plane faulting in the lower part of the Miocene section is required to produce the large-amplitude fold in the Neogene section that overlies the relatively flat upper basement contact. Lower Pliocene units do not thin greatly across the Lompoc structure in GSI-120, indicating that much of the structural relief of the fold formed after the lower Pliocene units were deposited. High-resolution line SM-82 (Figure 11, shot points 1162 to 1177)

indicates that units as young as late Pliocene are folded, although Pleistocene deposits do not appear to be measurably deformed.

Lines GSI-121 and Fairfield SM-74

Line GSI-121 shows the southernmost part of the Lompoc structure (shot points 160 to 260). The amplitude of the structure has diminished greatly from line GSI-120, 2 kilometers to the northwest. In line GSI-121, the Lompoc structure consists of two small anticlines within the Neogene section. Miocene through upper Pliocene sediments are affected by the folds, but Pleistocene deposits truncate folded upper Pliocene deposits (Figure 12, shot points 1177 and 1167 to 1170) and do not appear to be folded.

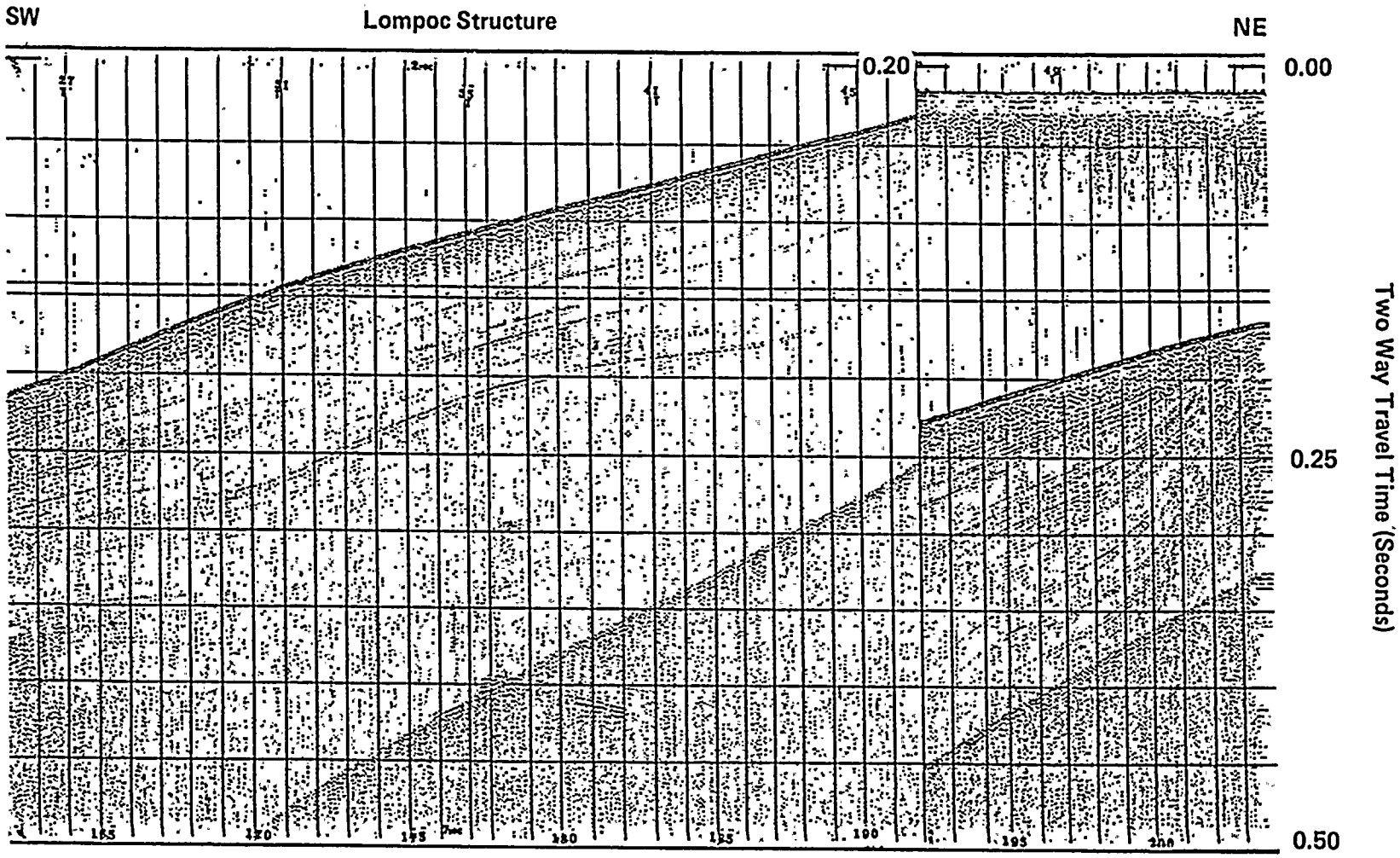

Figure 1. Fairfield Survey, Line SM-120

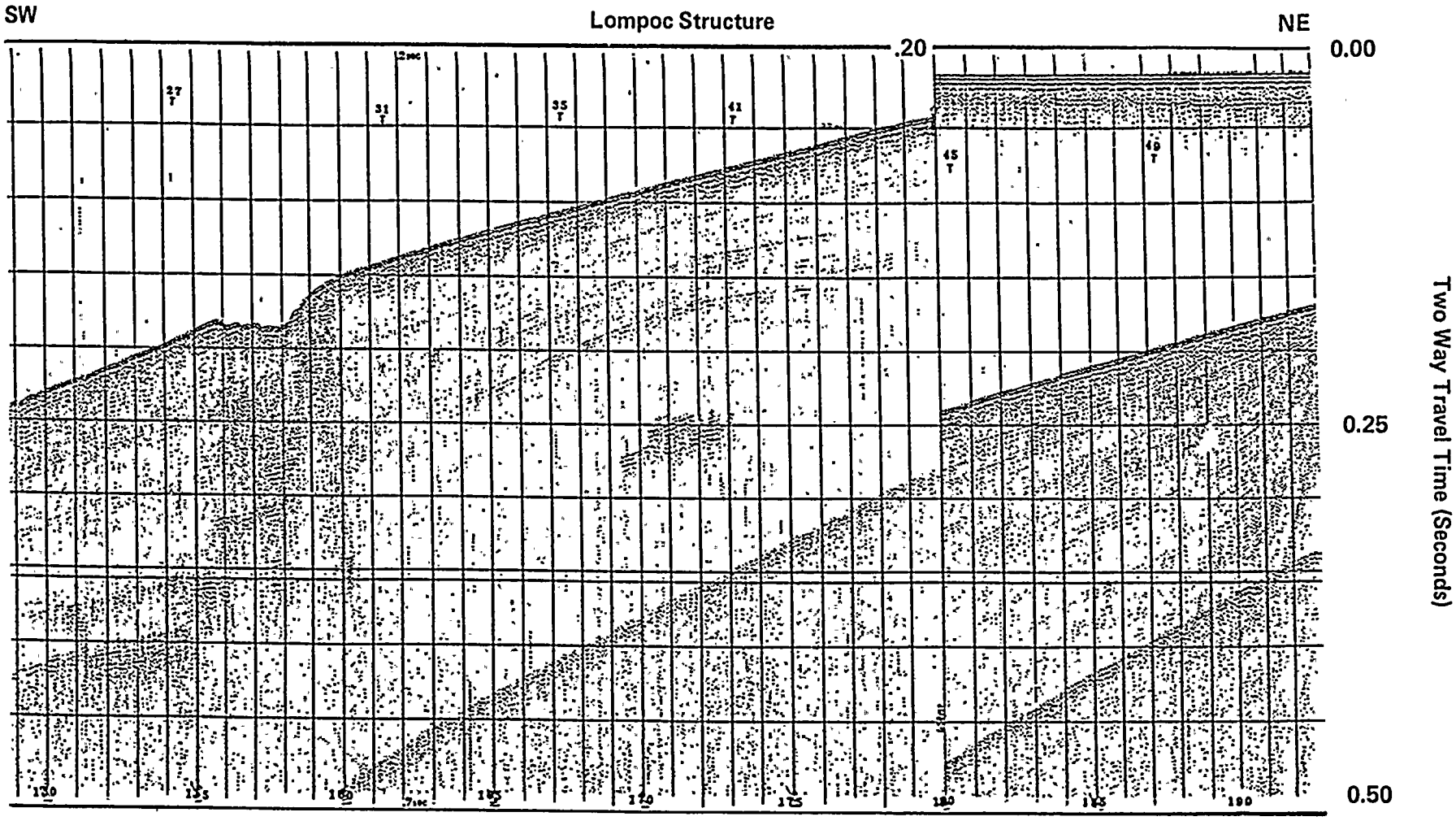

Figure 2. Fairfield Survey, Line SM-118

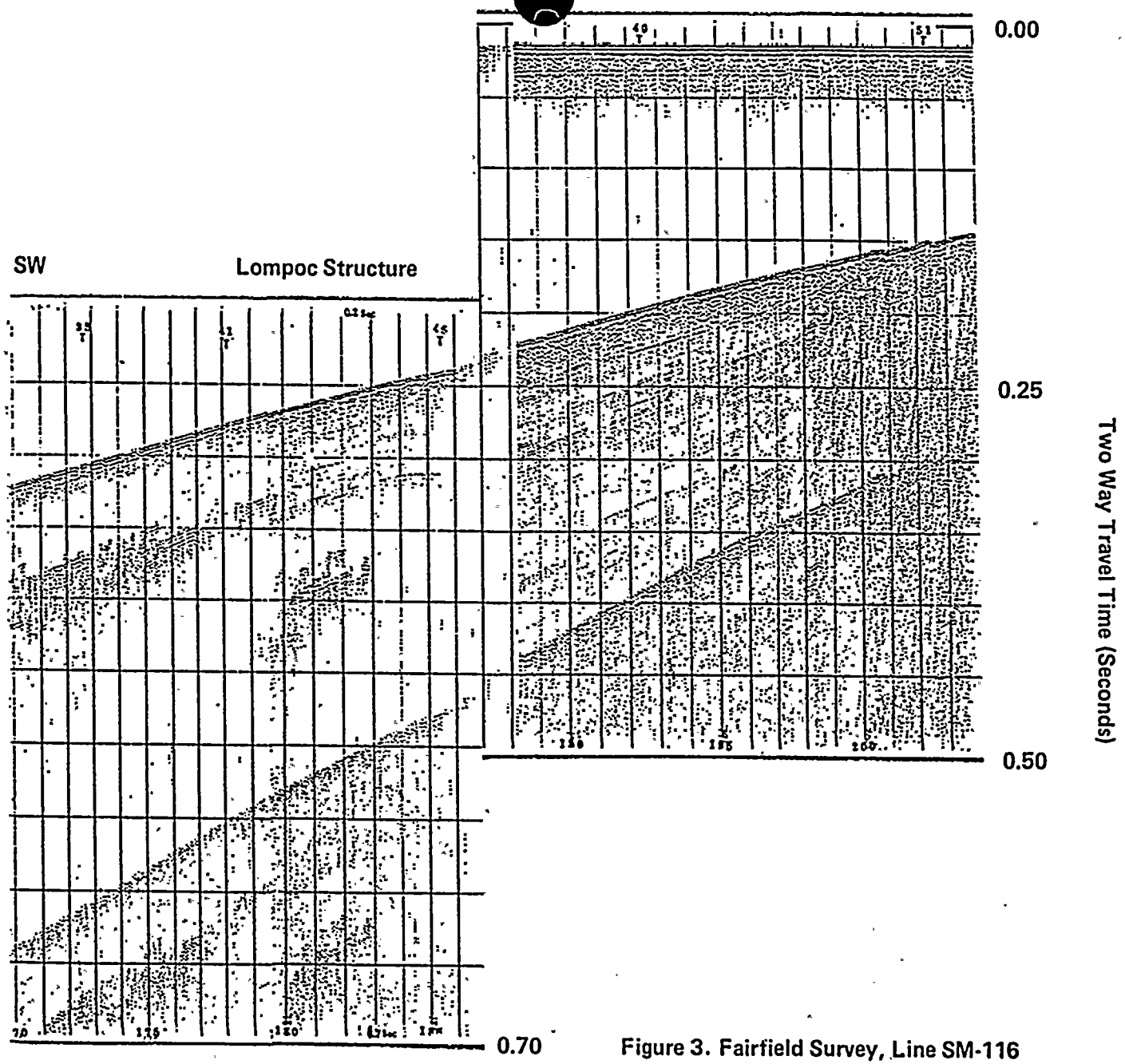

Figure 3. Fairfield Survey, Line SM-116

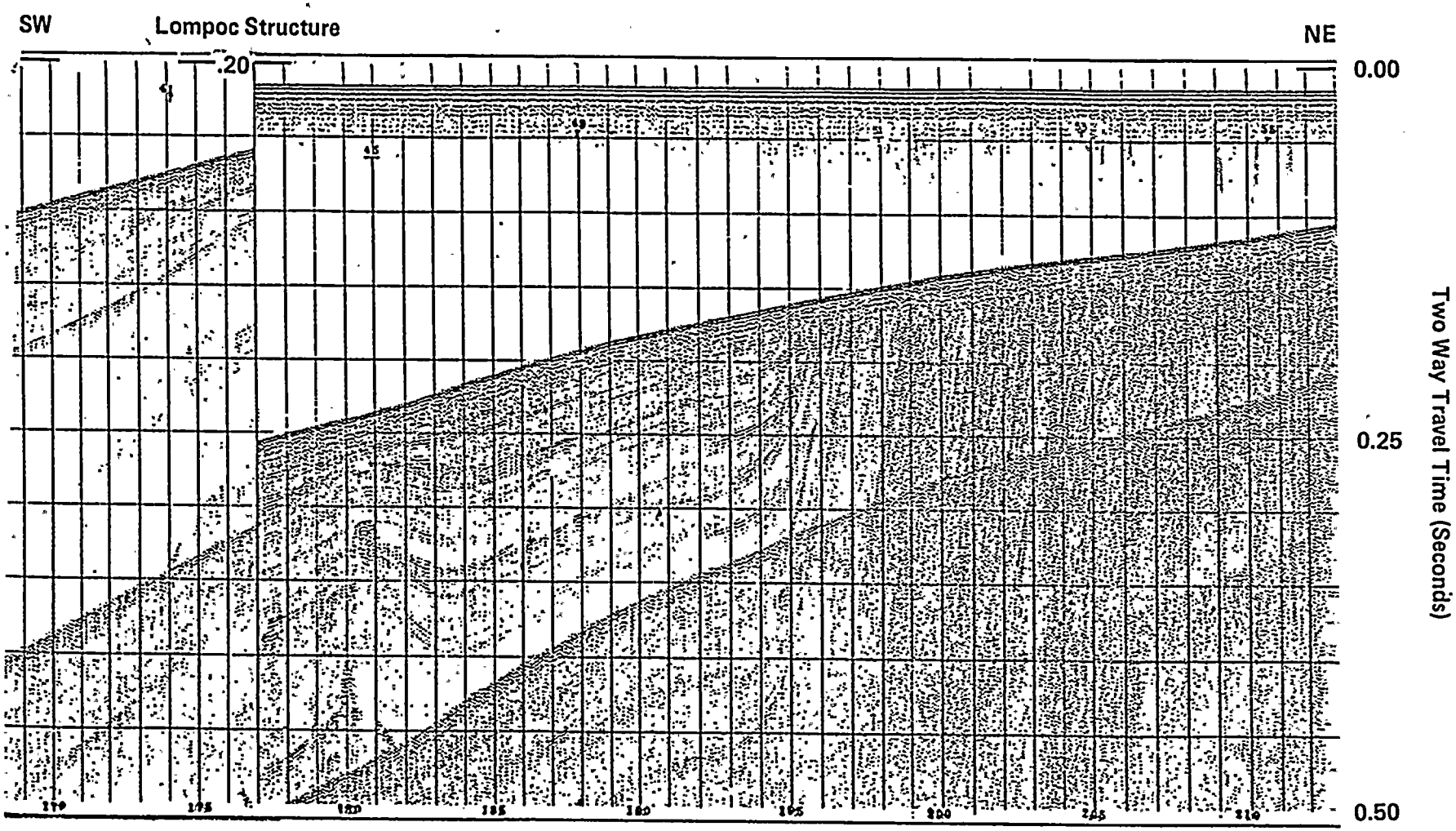

Figure 4. Fairfield Survey, Line SM-114

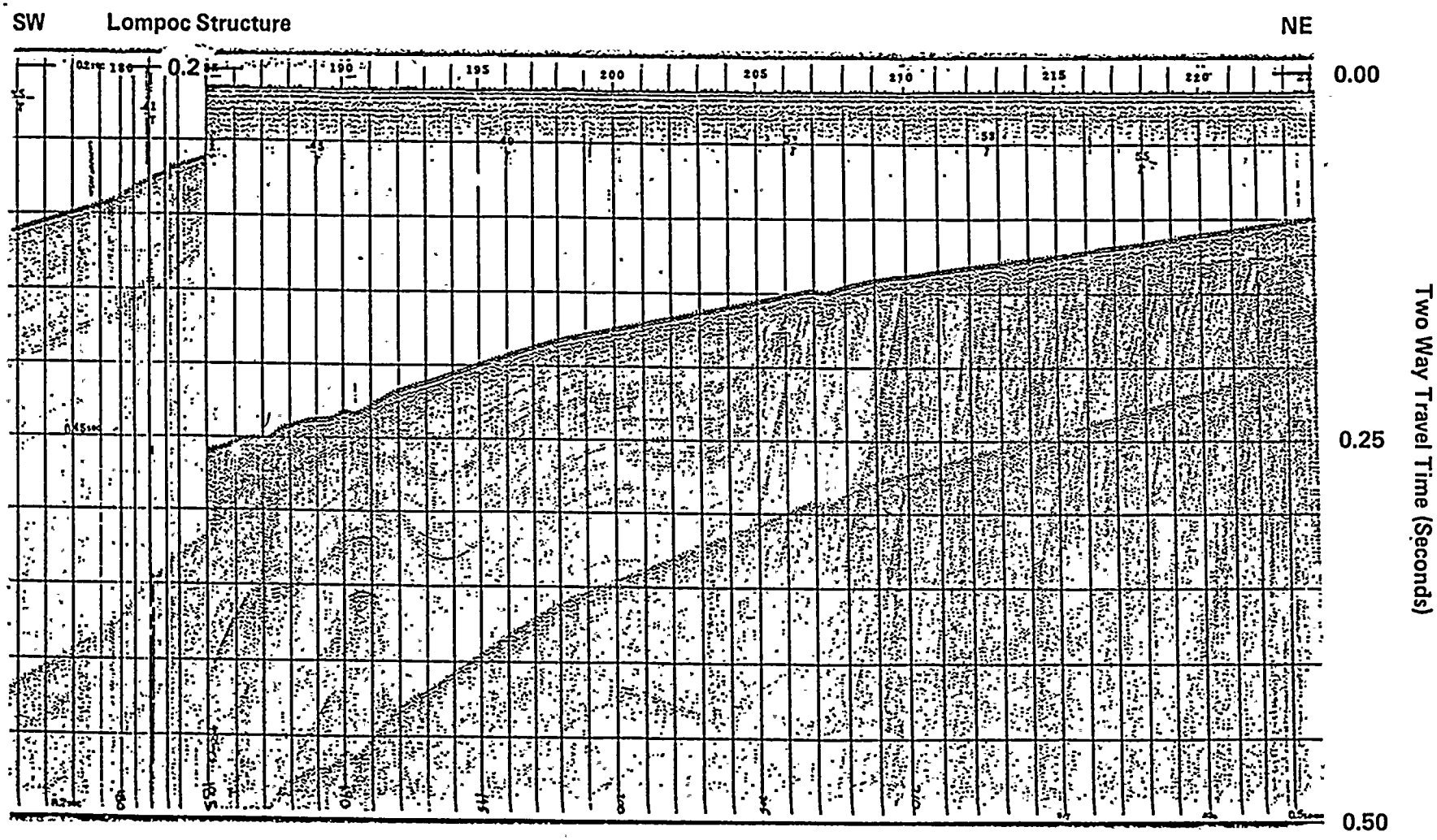

Figure 5. Fairfield Survey, Line SM-112

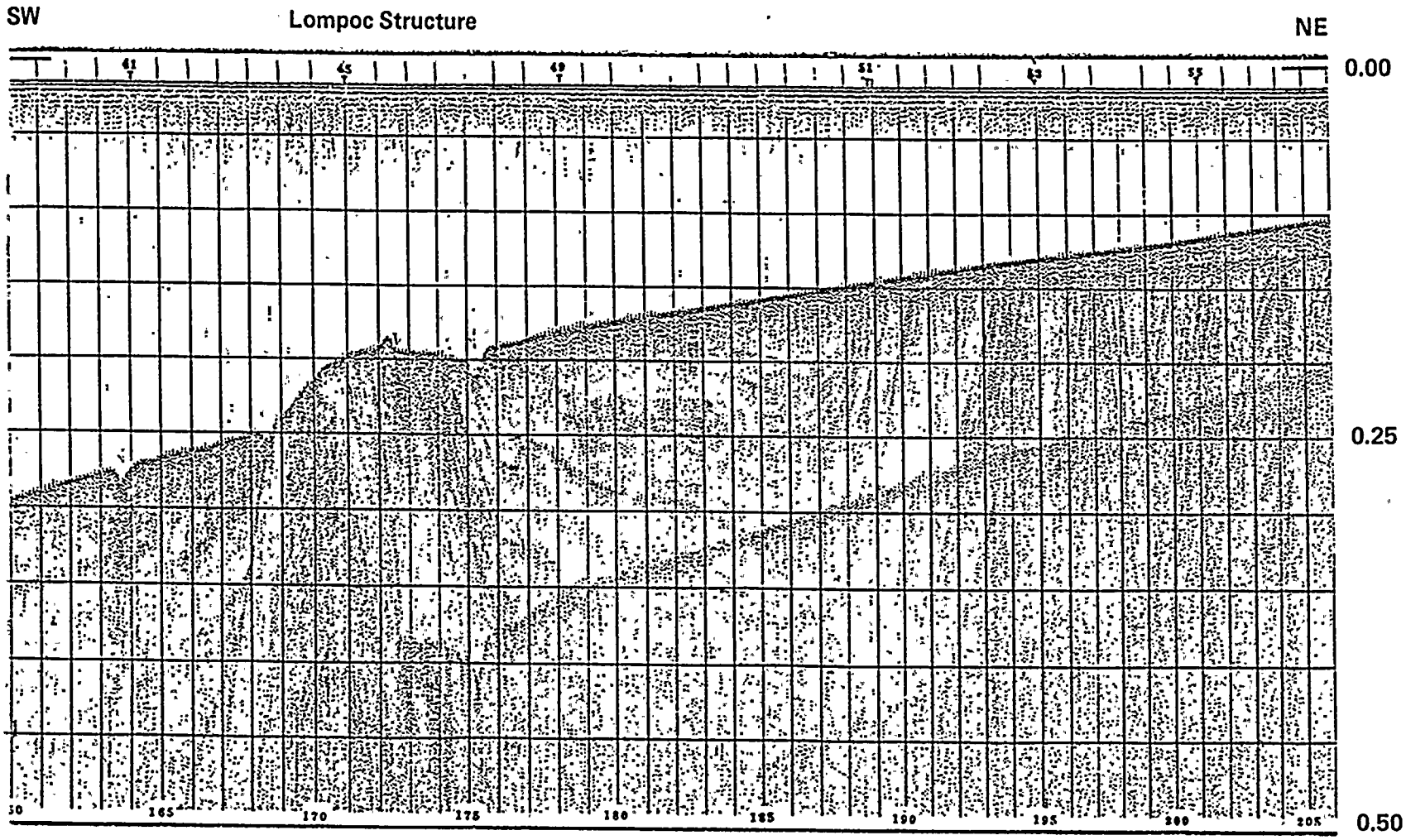

Figure 6. Fairfield Survey, Line SM-108

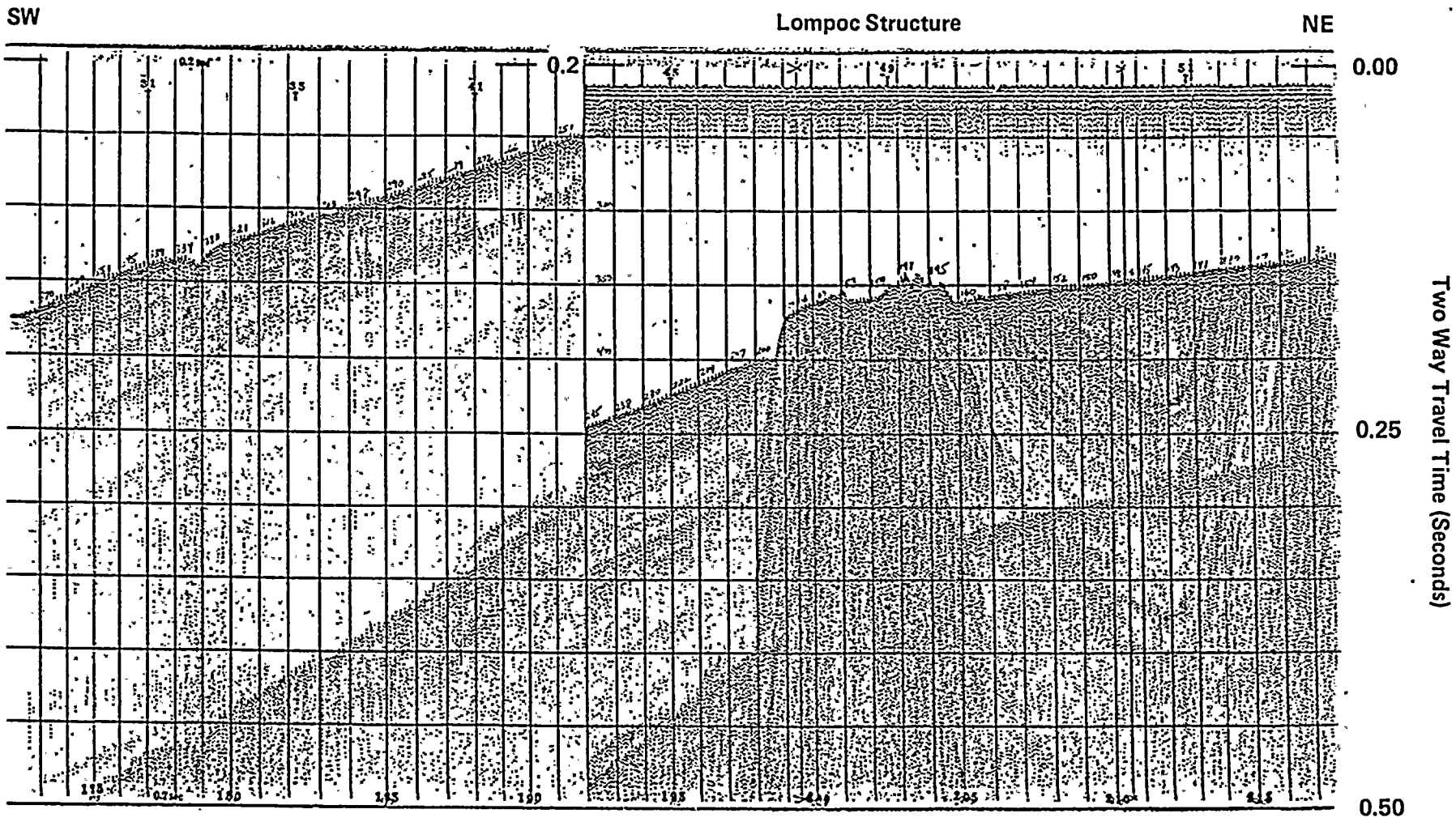

Figure 7. Fairfield Survey, Line SM-104

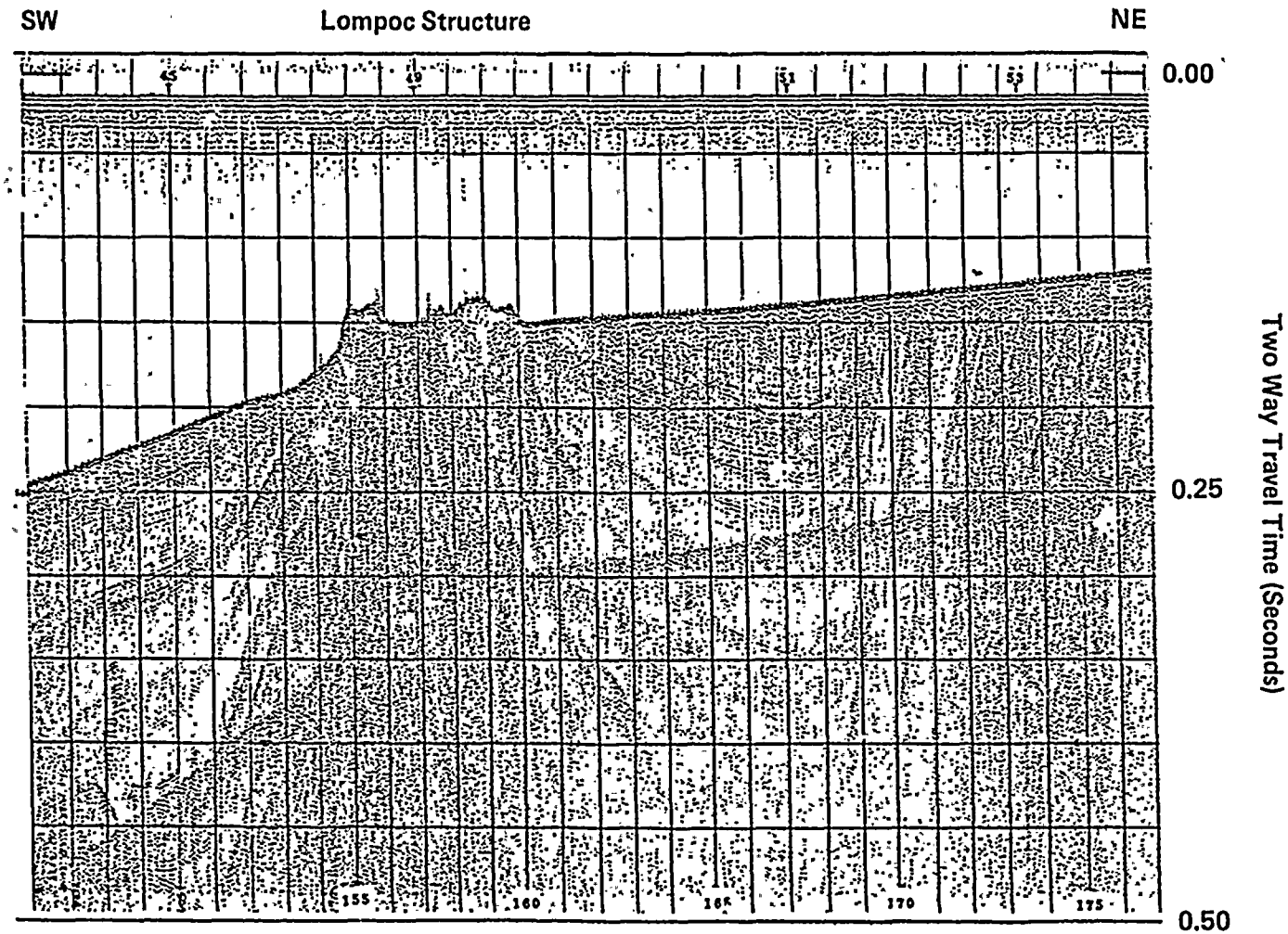

Figure 8. Fairfield Survey, Line SM-102

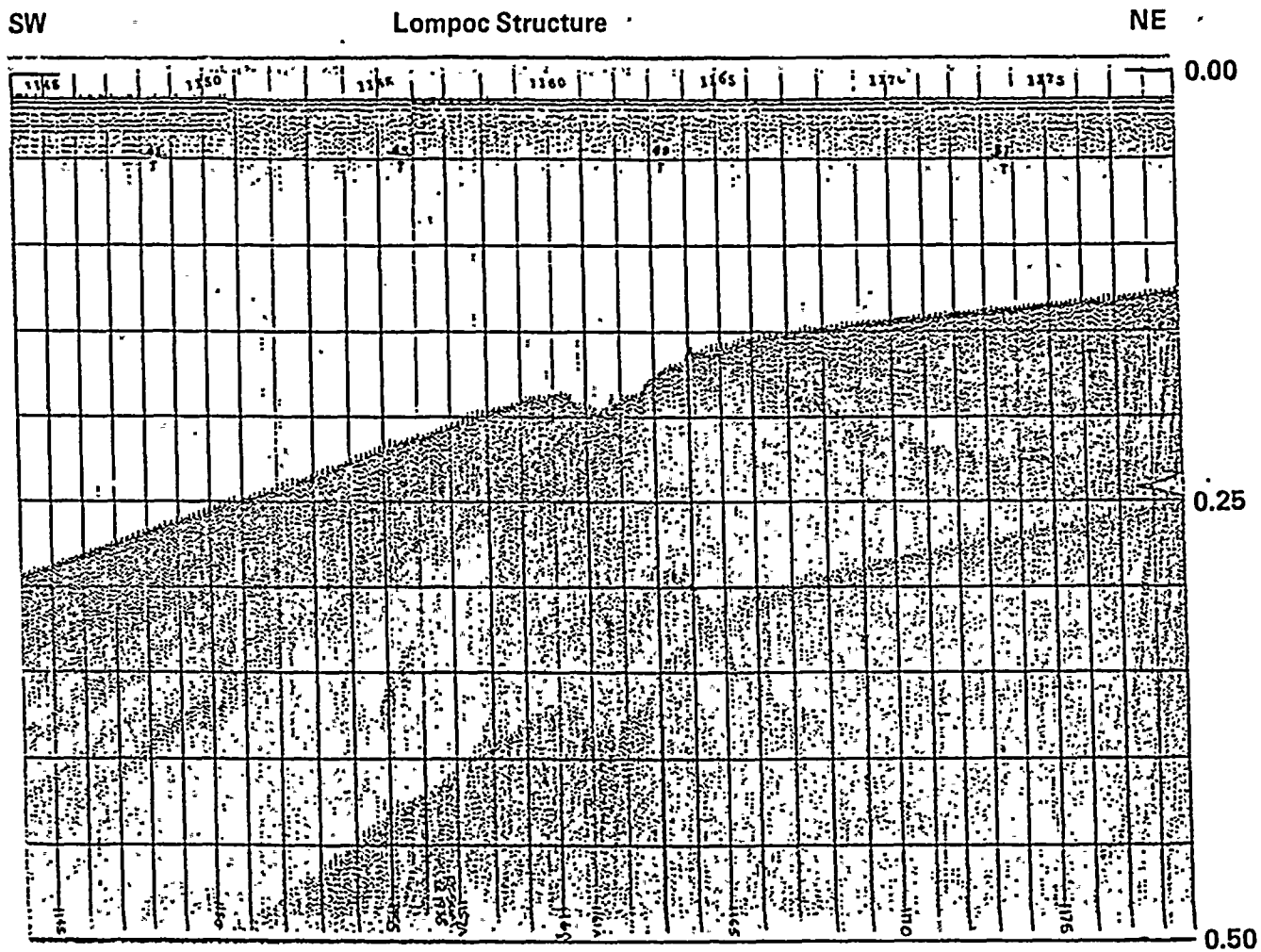

Figure 9. Fairfield Survey, Line SM-96

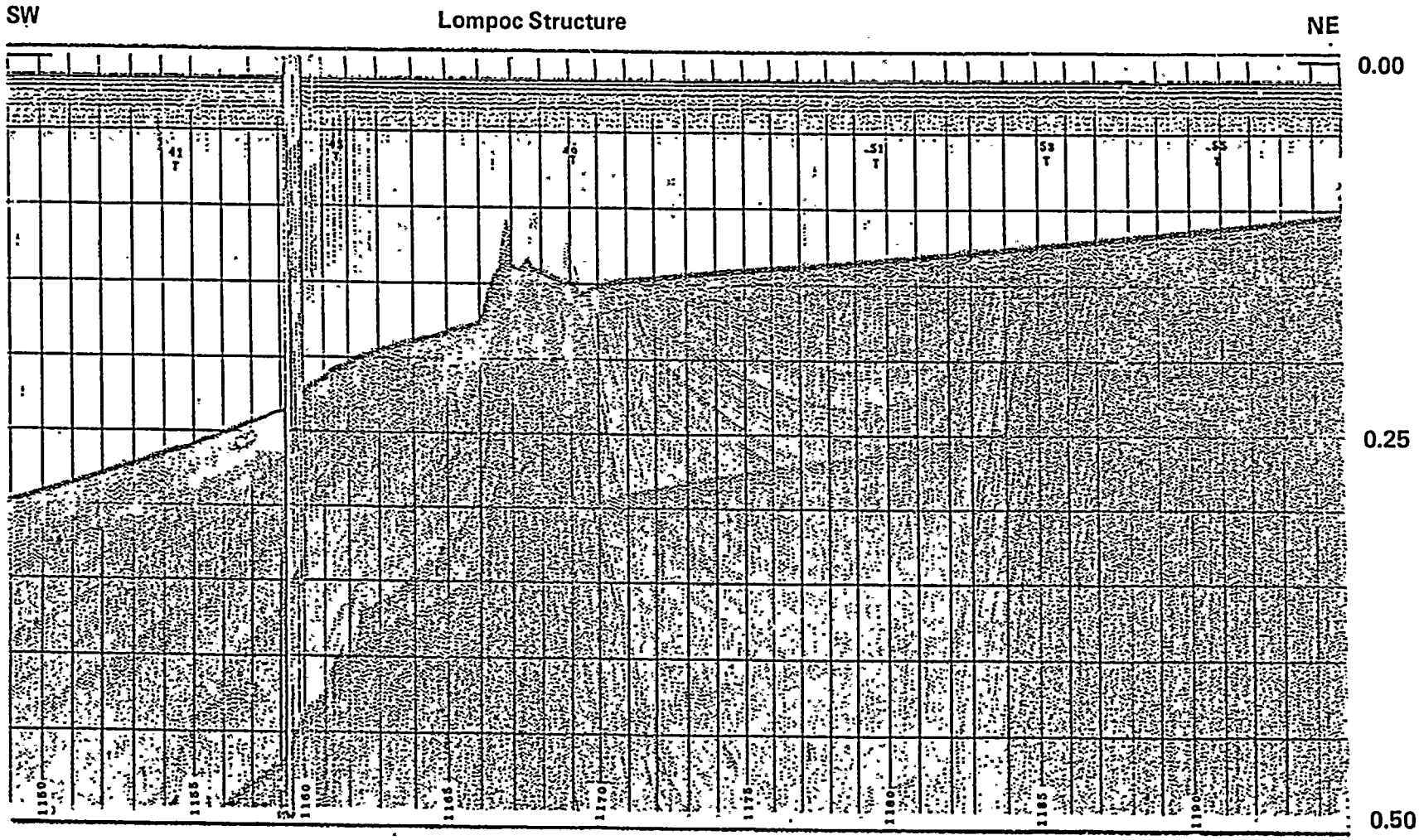

Figure 10. Fairfield Survey, Line SM-92

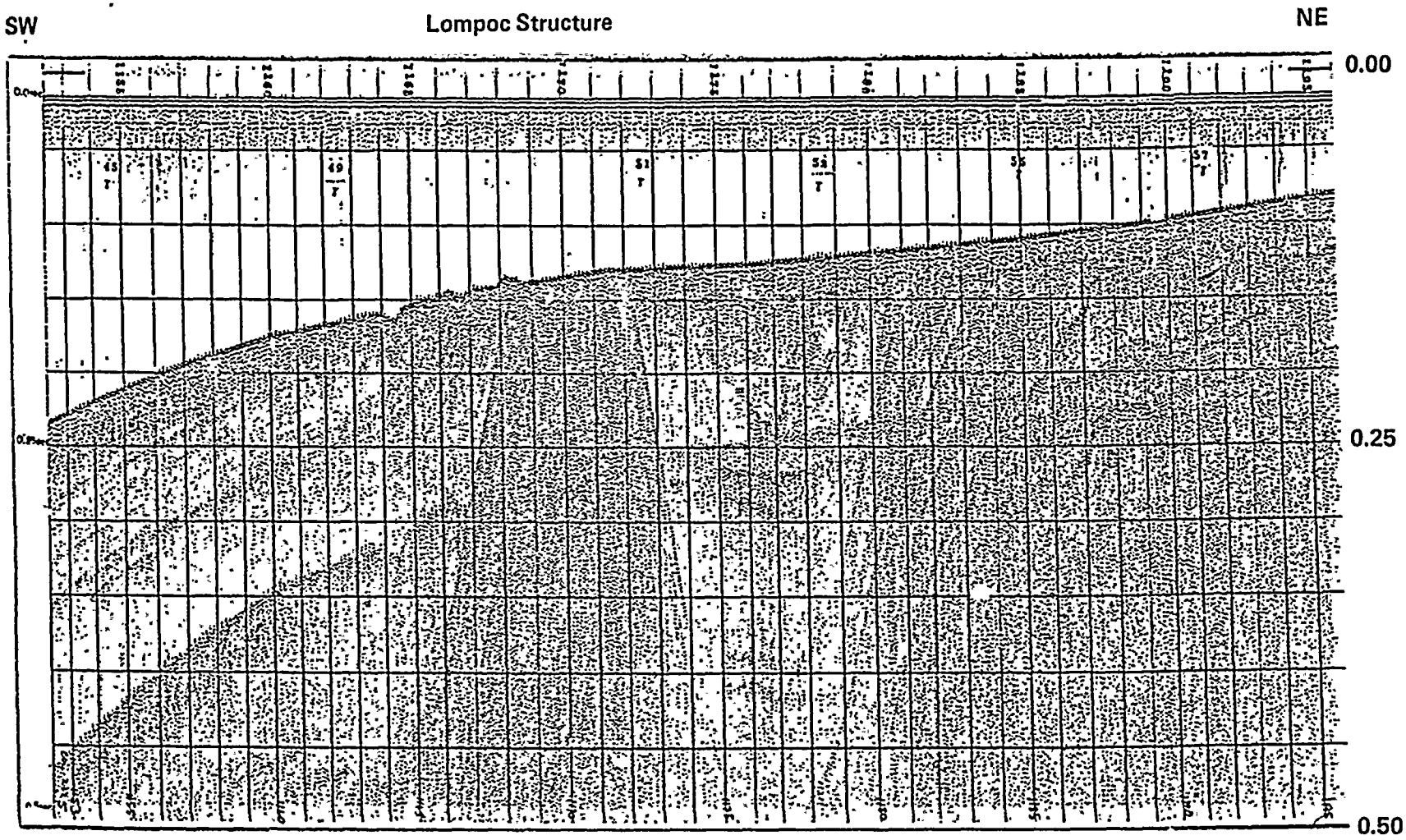

Figure 11. Fairfield Survey, Line SM-82

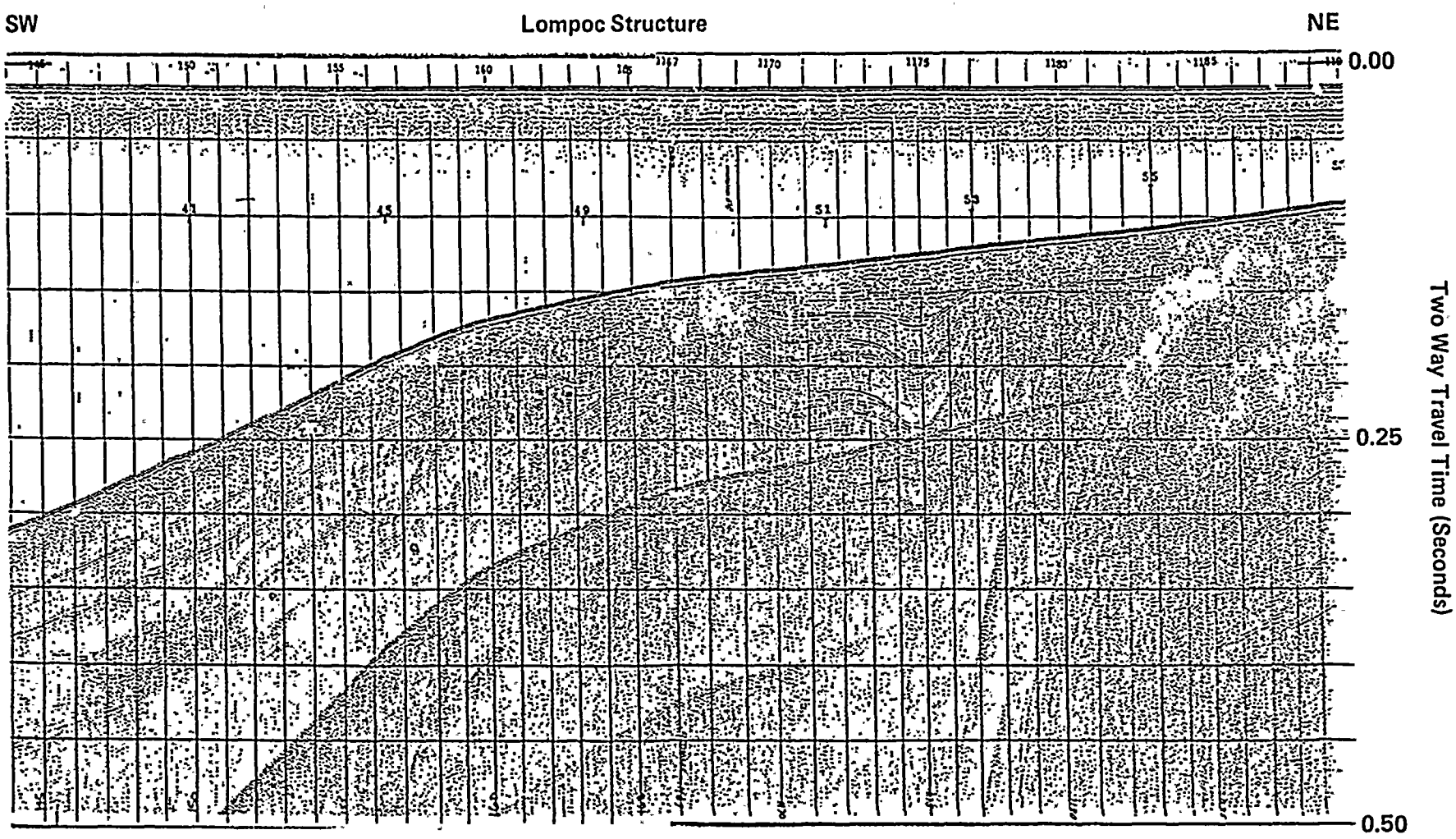

Figure 12. Fairfield Survey, Line SM-74

OVERSIZE DOCUMENT PAGE PULLED

SEE APERTURE CARDS

NUMBER OF OVERSIZE PAGES FILMED ON APERTURE CARDS 1

APERTURE CARD/HARD COPY AVAILABLE FROM

RECORDS AND REPORTS MANAGEMENT BRANCH

RESPONSE TO QUESTION 46

Question 46

Confirming the method that was used to relocate the 1927 Lompoc earthquake by using it for other events in the region that have been located independently would provide confidence as to the accuracy of the relocation. Using the same technique as discussed in the text and shown in Figure 2-27, locate other earthquake.

Location of the Lompoc Earthquake with respect to the Santa Lucia Banks Earthquake

The November 5, 1969, Santa Lucia Banks earthquake is ideally suited for use as a master event for the location of the Lompoc earthquake because of the proximity and similarity in focal mechanism between the two events. The location of the Santa Lucia Banks earthquake, as given by Gawthrop (1975), is shown in Figure Q46-1 and is estimated to have an uncertainty of less than 10 kilometers. The focal depth of the earthquake was estimated from depth phases to be 8 kilometers (Helmberger, personal communication, 1989); this depth is similar to the focal depth of 10 kilometers estimated for the 1927 Lompoc and 1983 Coalinga earthquakes. The earthquake had an estimated body wave magnitude of m_b = 5.8 (USCGS; ISC), and a seismic moment of 1.5×10^{25} dyne-centimeters estimated from P_{nL} waves (Helmberger, personal communication, 1989).

We have used SSS-S and S-P time differences to estimate the location of the Lompoc earthquake with respect to the Santa Lucia Banks earthquake. The S-P interval that was used was measured from the onset time of P, which is clear for both events, to the first large peak of the S wave. We chose this peak rather than attempt to identify the S onset because the S waves are dominated by SV, so their onsets are contaminated by S to P conversions. The S-P times of the Lompoc and Santa Lucia Banks earthquakes are identical, as shown in Figure Q46-2. The location of the Lompoc earthquake with respect to the Santa Lucia Banks earthquake, according to this measurement, is on the small circle centered on DeBilt and drawn through the Santa Lucia Banks epicenter. The location of the Lompoc earthquake is established as the intersection of this arc with the Santa Barbara arc.

As before, we have used SSS-S times rather than SS-S times because the SSS phase is larger than the SS phase on the DeBilt seismograms, and does not have the phase-shift with respect to S that the SS phase contains. The difference in SSS-S interval between the Lompoc and Santa Lucia Banks earthquakes was measured by aligning the two S waves using cross-correlation, and then finding the time difference between the two SSS waves using cross-correlation, as shown in Figure Q46-3. The SSS-S time of the Lompoc event is 0.5 second greater than that of the Santa Lucia Banks event, placing the Lompoc earthquake about 12 kilometers south of the location derived from S-P data. The proximity of the Lompoc and Santa Lucia Banks earthquakes is reflected in the similarity of their waveforms; this is particularly evident when the Santa Lucia Banks record is lowpass filtered (Figure Q46-3) to provide a better comparison with the larger Lompoc earthquake. This provides further confirmation of the proximity of the two events.

Refined Location of the Lompoc Earthquake with respect to the Coalinga Earthquake

We have used the measurement methods described above to refine our location of the Lompoc earthquake relative to the Coalinga earthquake. We first used the known locations of the Coalinga and Santa Lucia Banks earthquakes (1.85 degrees apart) and their measured SSS-S time difference (9.3 seconds) to estimate the relation between SSS-S time difference and distance from Coalinga (5.0 seconds per degree). Applying this to the SSS-S time difference of 10.1 seconds between the Coalinga and Lompoc earthquakes, as measured using the correlation method, places the Lompoc earthquake about 20 kilometers south of the S-P location and about 10 kilometers south of the SSS-S location with respect to the Santa Lucia Banks earthquake. There is a closure error in the differences in the three SSS-S times (0.5, 9.3, -10.1) that is due to noise in the seismograms. This closure error results in a discrepancy of 10 kilometers between the SSS-S locations of the Lompoc earthquake with respect to the Santa Lucia Banks and Coalinga earthquakes, and provides an indication of the level of uncertainty that is entailed in the measurement method.

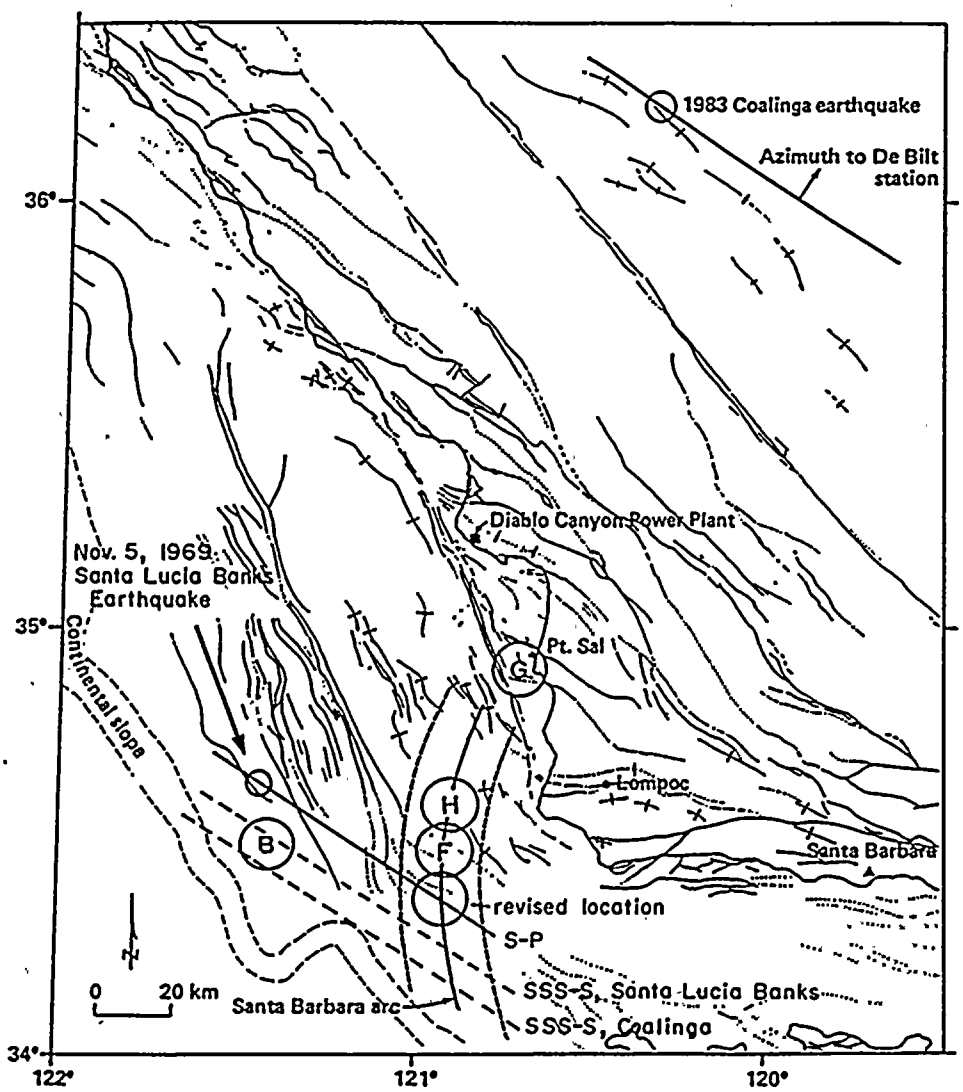

EXPLANATION

1927 Lompoc Earthquake Epicenters

(B) Byerly (1930) (H) Hanks (1979) (G) Gawthrop (1978) (F) Final Report

(○) Revised Location

Arcs drawn from De Bilt and Santa Barbara seismograph stations

Note: Modified from Figure 2-24 of the Final Report.

Figure Q46-1

Constraints on the location of the 1927 Lompoc earthquake from differential travel times of P, S, and SSS phases at DeBilt with respect to the 1969 Santa Lucia Banks and 1983 Coalinga earthquakes, and from the S-P times of aftershocks recorded at Santa Barbara.

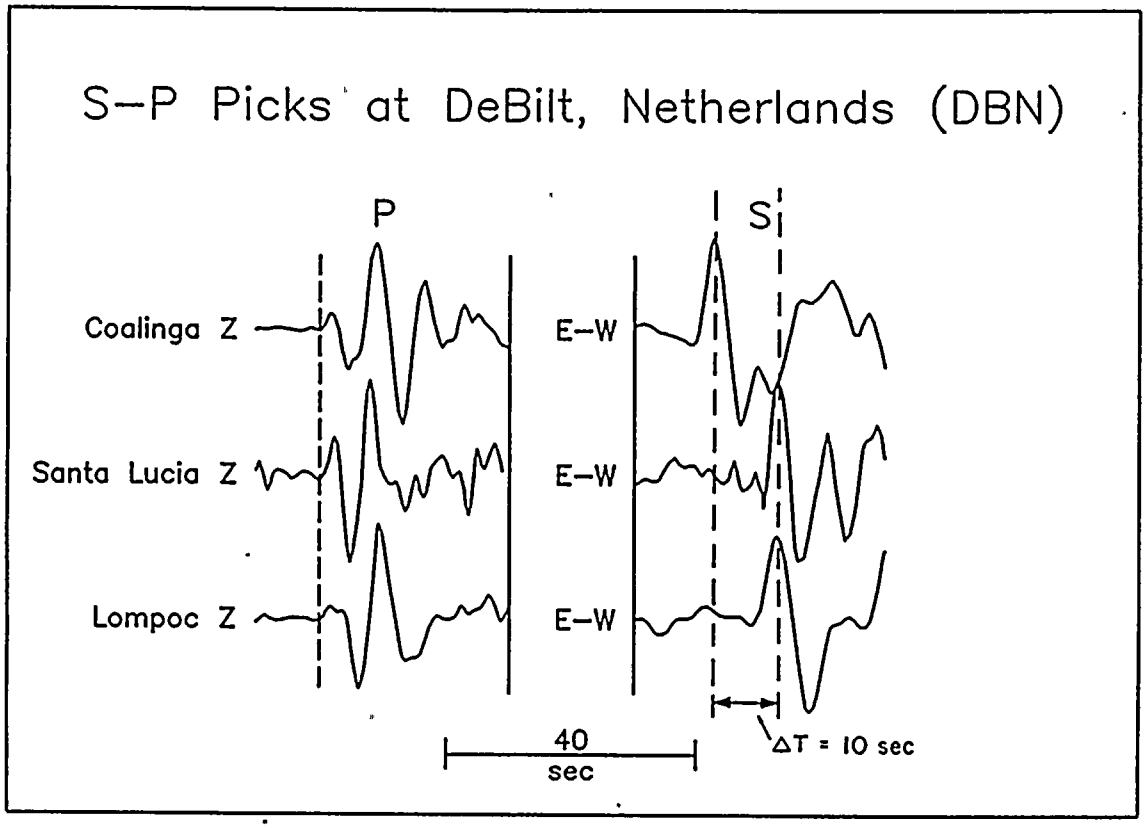

Figure Q46-2

Comparison of S-P times of the 1927 Lompoc, 1969 Santa Lucia Banks, and 1983 Coalinga earthquakes.

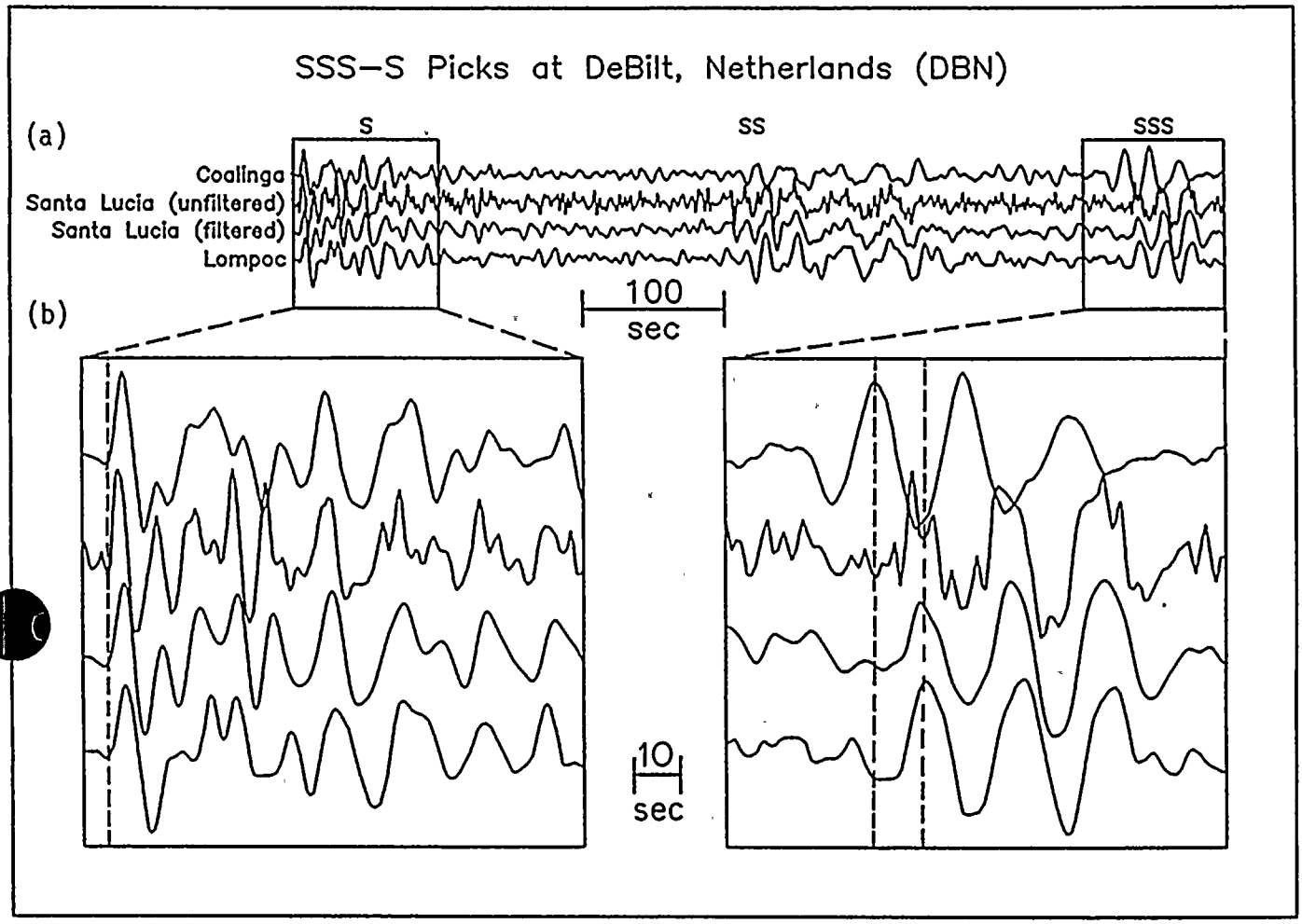

Figure Q46-3

(a) Comparison of shear wave seismograms of the 1927 Lompoc, 1969 Santa Lucia Banks, and 1983 Coalinga earthquakes, showing strong similarity in waveform and timing of the Lompoc and Santa Lucia Banks events. (b) Comparison of SSS-S times of the three earthquakes. In the lower right box, the times of the first peak of the SSS wave for the Santa Lucia Banks and Lompoc events are seen to be similar, and approximately 10 seconds later than that for the Coalinga event.

The method of estimating S-P time uses simple time picks rather than cross-correlations, and is thus not subject to closure error when the Coalinga earthquake is included in the analysis. The fact that the S-P times of the Lompoc and Santa Lucia Banks earthquakes are identical means that they both have the same difference in S-P time with respect to the Coalinga earthquake (10 seconds), and their distances from Coalinga are thus identical. The S-P location of the Lompoc earthquake with respect to the Coalinga earthquake is thus identical to the S-P location of the Lompoc earthquake with respect to the Santa Lucia Banks earthquake.

Revised Location

Given the uncertainties discussed below, we conclude that the distance of the Lompoc earthquake from DeBilt is not significantly different from the distance of the Santa Lucia Banks earthquake from DeBilt. Together with the Santa Barbara arc, the DeBilt arc through the Santa Lucia Banks epicenter gives a revised location for the Lompoc Earthquake of 34.35°N, 120.9°W. This location is about 15 kilometers south of that given in the Final Report, but is well within the uncertainty of that estimate.

Estimate of Uncertainty in Location

The uncertainty in location of the Lompoc earthquake cannot be less than that of the master events used in its location. For the Santa Lucia Banks earthquake, this uncertainty is estimated to be less than 10 kilometers; for the Coalinga earthquake, it is a few kilometers. In addition to this uncertainty is the variability in location obtained using different master events and different phase pairs (Figure Q46-1), which is 10 kilometers about the average location. Differences in such parameters as focal depth, earth structure, and source functions of the earthquakes are expected to cause additional uncertainty. We estimate the combined uncertainty of the location to be 25 kilometers about the revised location.

References

Byerly, P., 1930, The California earthquake of November 3, 1927: *Bulletin of the Seismological Society of America*, v. 68, p. 53-66.

Gawthrop, W. H., 1978, Seismicity and tectonics of the central California coastal region: in Silver, E. A., and Normack, W. R., eds., San Gregorio-Hosgri fault zone, California, California Division of Mines and Geology, Special Report 137, p. 45-56.

Hanks, T. C., 1979, The 1927 Lompoc, California earthquake (November 4, 1927; M=7.3) and its aftershocks: *Bulletin of the Seismological Society of America*, v. 69, p. 451-462.

RESPONSE TO QUESTION 16

February 1989

This volume is part of a set that responds to 47 questions asked of PG&E by the Nuclear Regulatory Commission (NRC) on December 13, 1988. The responses provide data requested to augment or clarify the Final Report of the Long Term Seismic Program submitted by PG&E to the NRC on July 31, 1988.

RESPONSE TO QUESTION 16

Question 16

Provide a complete discussion as to how the 84th percentile numerical modeling estimates were made and how they address the various types of modeling, parametric, and random uncertainties. Determine the quantative goodness of fit measures for the numerical modeling procedures based upon the comparison of the numerical simulations with actual data from the Imperial Valley, Coalinga, Nahanni, and Whittier Narrows earthquakes referenced in the LTSP Final Report.

Method

The uncertainty in the response spectrum derived by numerical modeling is divided into three kinds: modeling, parametric, and random. The modeling uncertainty and random uncertainty are estimated jointly by measuring the goodness of fit of the recorded and simulated response spectra in the validation procedure. The parametric uncertainty is estimated by including variations in model parameters in the ground motion simulations for the Diablo Canyon site. The overall uncertainty is obtained by combining these two uncertainty estimates.

The modeling uncertainty is due to differences between the actual processes that generate strong ground motion and the simulation of those processes in the numerical procedure. It includes several aspects of the rupture process that are difficult to observe and for which reasonable assumptions are made. These include the rupture velocity (0.8 times the shear wave velocity); the slip velocity (given by the relation of Geller (1976)); the degree of randomness of rupture velocity and slip velocity (3 sigma); the fault element size (4 x 3 kilometers); the empirical source functions (a suite of recordings of the Imperial Valley aftershock was used throughout); and a procedure for estimating the slip distribution model (based on slip models and the inverse correlation between slip distribution and aftershocks summarized by Mendoza and Hartzell (1988)).

An alternative to the validation procedure that we used would be to allow certain aspects, such as rupture velocity, to vary to optimize the fit. The measure of goodness of fit would then exclude (at least to some extent) uncertainty in the rupture velocity; rupture velocity would then become a parametric uncertainty to be evaluated at the Diablo Canyon site by including simulations having different rupture velocities. However, this alternative course was not taken. We chose to measure the uncertainty in ground motions due to uncertainty in rupture velocity by fixing the rupture velocity in our modeling procedure and then measuring the resulting discrepancy (together with discrepancies related to other aspects of the model) between the recorded and simulated ground motions. To then also include rupture velocity as a parametric uncertainty would be to count it twice.

A second kind of uncertainty that is included in measures of goodness of fit between recorded and simulated motions is that due to randomness. Detailed aspects of earthquake source and wave propagation processes exist that cannot be modeled deterministically using our current level of knowledge; we treat these as random, and expect them to give rise to discrepancies between recorded and simulated motions in addition to those due to modeling uncertainty. In recognition of this randomness, we have included randomness in the way we model rupture velocity, slip velocity, and radiation pattern, and have used empirical source functions that contain scattering effects. The modeling and random uncertainties, as estimated by goodness of fit measurements between recorded and simulated motions, are not separable.

In contrast with the aspects of the simulation procedure enumerated above that are treated as modeling and random uncertainty, certain other aspects are most naturally treated parametrically. In the validation procedure, we have reasonably good knowledge of the location of the hypocenter, the location of the boundaries of the rupture surface, and the location of the recording stations, as well as some knowledge of the slip distribution. These geometrical parameters determine such aspects as whether the rupture is predominantly unilateral or bilateral, and where the asperities are located. Because these parameters are known in the validation procedure, measures of goodness of fit between recorded and simulated ground motions will not include a significant contribution due to uncertainty in these parameters. It is therefore necessary to include a measure of these uncertainties in the simulations at the Diablo

Canyon site. This was done by performing simulations for a variety of rupture modes (bilateral and unilateral) and positions of the fault rupture (and the slip-distribution asperities on it) with respect to the site.

From the preceding discussion, it is evident that there were no free parameters involved in the validation procedure that we adopted: there were unobserved aspects for which reasonable assumptions were made and incorporated into the modeling procedure, and there were known geometrical parameters constrained by data. In the simulations at the Diablo Canyon site, the unobserved aspects were again fixed as part of the modeling procedure, and the geometrical parameters, being unknown for future earthquakes, were varied.

Estimate of Modeling and Random Uncertainty from Goodness of Fit with Data

Multiple recordings of three events were used in the estimation of goodness of fit. These include the 1979 Imperial Valley event (six stations), the 1985 Nahanni event (three stations), and the 1987 Whittier Narrows event (nine stations). In all cases, recordings of an aftershock of the Imperial Valley event were used as empirical source functions. We checked to see whether this caused significantly better fit for the Imperial Valley event than for the other events, but it did not. This justifies the inclusion of the Imperial Valley event with the other two events in the estimation of goodness of fit. Measurements for individual recordings and response frequencies are shown in Figure Q16-1. The mean bias and standard error of individual response frequencies averaged over all recordings is shown in Figure Q16-2.

The main frequency band of interest is 3.0 to 8.5 Hz. The natural logarithm of the observed and calculated response spectra were averaged over this frequency band. The residual for each recording station is defined as the difference between the observed and calculated frequency averaged spectra. The mean residual represents the bias of the model. The mean residuals for each event are as follows:

Earthquake	Bias	Standard Deviation	No. of Stations
Imperial Valley	-0.164	0.226	6
Nahanni	-0.154	0.660	3
Whittier Narrows	-0.094	0.318	9

Averaged over the frequency range of 3.0 to 8.5 Hz, the mean bias is -0.128; the standard error of a single observation is 0.34 on the natural logarithm of response spectral acceleration. The negative bias indicates that the simulation procedure is overpredicting the recorded frequency averaged spectral acceleration by about 14 percent.

Estimate of Parametric Uncertainty in Simulations for Diablo Canyon Site

The model parameters that were varied parametrically in the 116 simulations at the Diablo Canyon site include the rupture mode (unilateral or bilateral) and the location of the rupture surface (and the asperities on it) with respect to the site. Two additional aspects were also varied, but these variations do not belong in and are not included in the estimate of parametric uncertainty. First, two different sets of empirical source functions (Imperial Valley and Coalinga) were used. However, because the estimate of modeling uncertainty already includes a component due to differences between the Imperial Valley source functions and the actual process as contained in the data, we excluded variability in source functions (between Imperial Valley and Coalinga) in the estimate of parametric uncertainty. Second, simulations were performed for three different fault mechanisms: strike-slip, oblique, and thrust. However, uncertainty in focal mechanism was considered to be an aspect of uncertainty in source specification, and was not treated as a parametric uncertainty in the ground motion modeling. Accordingly, individual estimates of parametric uncertainty were obtained for each of the three fault mechanisms. The standard deviation for strike-slip, oblique, and thrust mechanisms are 0.368, 0.389, and 0.288, respectively. These three mechanisms were assigned weights of 0.65, 0.30, and 0.05, respectively in the Final Report. A weighted variance estimate produces a parametric uncertainty standard deviation of 0.371.

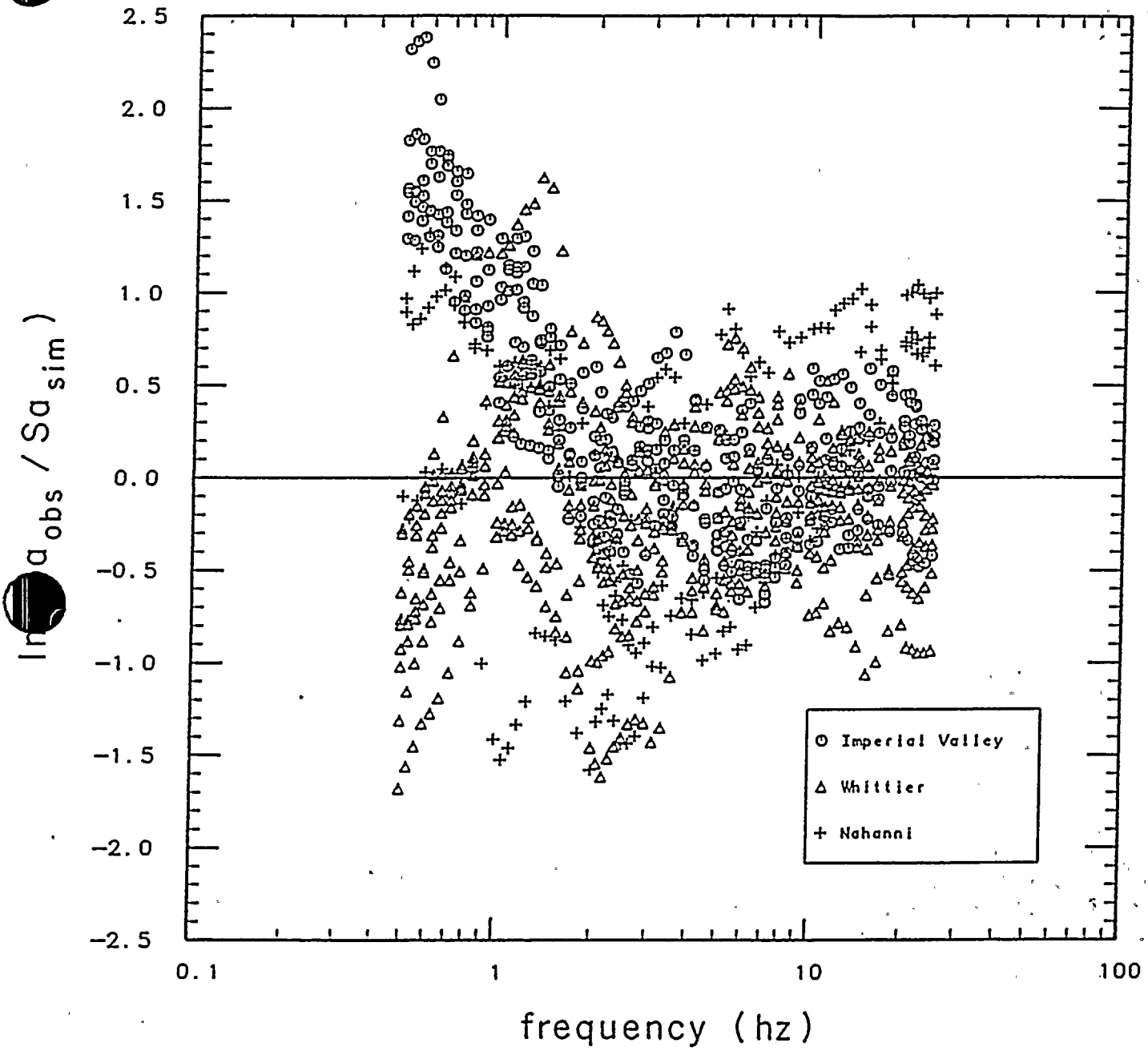

Figure Q16-1

Deviation between recorded and simulated horizontal response spectral acceleration at 5 percent damping for individual earthquake-station pairs.

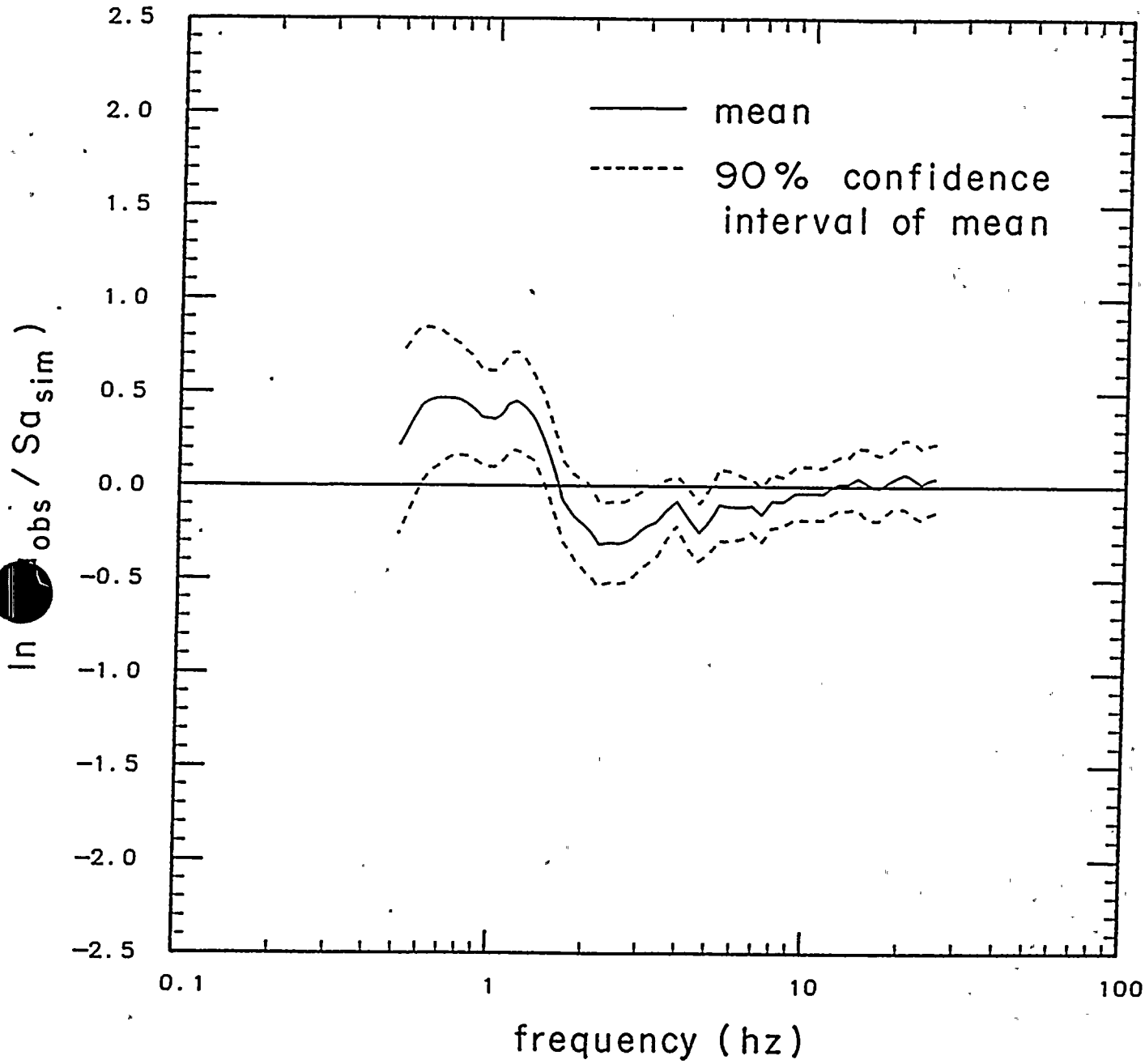

Figure Q16-2.

Deviation between recorded and simulated horizontal response spectral acceleration at 5 percent damping averaged over all earthquake-station pairs.

This estimate of the parametric uncertainty includes uncertainty in both the rupture mode and in rupture (and asperity) location. We can estimate the relative importance of these two parameters, but the fact that they are coupled prevents us from estimating their individual contributions to the overall parametric uncertainty. The uncertainty in rupture location leads to much larger variation in ground motion than the uncertainty in rupture mode. The standard deviations of the frequency averaged spectral acceleration due to uncertainty in rupture location and rupture mode are 0.380 and 0.110, respectively on the natural logarithm scale. Because these parameters are coupled, the simple (square root of the sum of the squares) combination of these values is inappropriate and would lead to an overestimate of the actual combined uncertainty of 0.371.

Overall Estimate of Uncertainty

The overall estimate of uncertainty in the deterministic response spectrum derived from numerical modeling was obtained by combining the modeling plus random uncertainty estimate (0.34) with the parametric uncertainty estimate (0.37). Taking the square root of the sum of the squares of the individual standard errors, we obtained a standard error of 0.50 in the frequency averaged spectrum. This corresponds to a factor of 1.65. The contributions of modeling plus random uncertainty and of parametric uncertainty are numerically similar.

Comparison of Overall Uncertainty Estimate with the 84th Percentile

The 84th percentile deterministic response spectrum obtained from numerical modeling was estimated using an abbreviated form of the method described above. In place of using an estimate of modeling and random uncertainty derived from the goodness of fit between recorded and simulated motions, we included two different sets of empirical source functions in the 116 simulations at the Diablo Canyon site. The result was a standard deviation of 0.49, compared with the value of 0.50 obtained using the method described here. These two values are very similar.

References

Geller, R. J., 1976, Scaling relations for earthquake source parameters and magnitudes: *Bulletin of the Seismological Society of America*, v. 66, p. 1501-1523.

Mendoza, C., and Hartzell, S. H., 1988, Inversion for slip-distribution using teleseismic waveforms: North Palm Springs, Borah Peak, and Michoacan earthquakes: *Bulletin of the Seismological Society of America*, v. 78, p. 1092-1111.

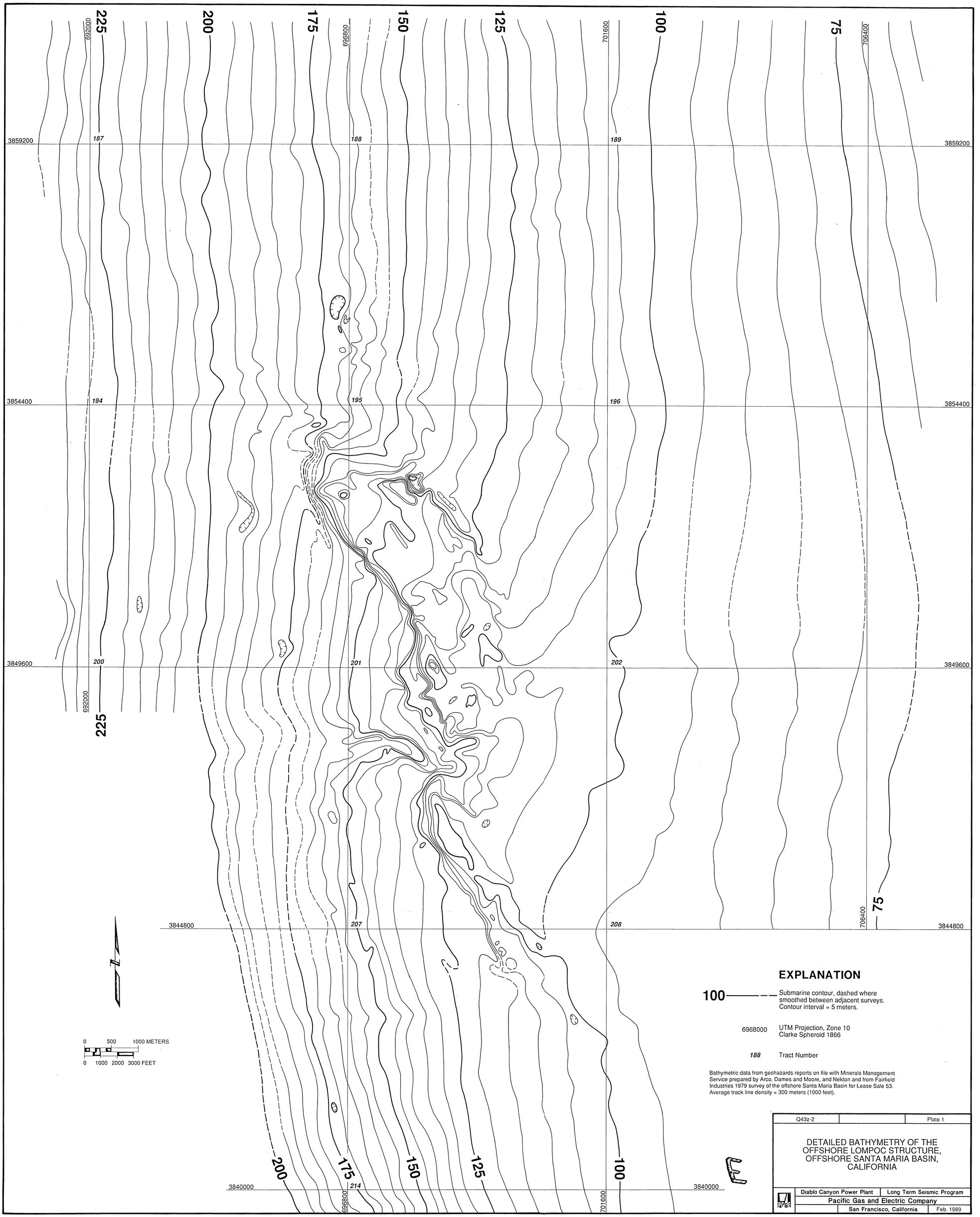

8903080423-01